Inorganic Chemistry

Article

pubs.acs.org/IC

Tellurotungstate-Based Organotin−Rare-Earth Heterometallic Hybrids with Four Organic Components

Qing Han,[†] Jian-Cai Liu,[†] Yue Wen,[†] Li-Juan Chen,*[,†] Jun-Wei Zhao,*[,†] and Guo-Yu Yang*[,‡]

[†]Henan Key Laboratory of Polyoxometalate Chemistry, Institute of Molecular and Crystal Engineering, College of Chemistry and Chemical Engineering, Henan University, Kaifeng, Henan 475004, People's Republic of China

[‡]MOE Key Laboratory of Cluster Science, School of Chemistry, Beijing Institute of Technology, Beijing 100081, People's Republic of China

Supporting Information

ABSTRACT: A family of unprecedented tellurotungstate-based organotin−rare-earth (RE) heterometallic hybrids $[H_2N(CH_3)_2]_6H_{12}Na_2$ $\{[Sn(CH_3)W_2O_4(IN)]$-$[(B\text{-}\alpha\text{-}TeW_8O_{31})RE(H_2O)\ (Ac)]_2\}_2\cdot 25H_2O$ [RE = Ce^{III} (**1**), Pr^{III} (**2**), Nd^{III} (**3**), Sm^{III} (**4**), Eu^{III} (**5**), Gd^{III} (**6**), Tb^{III} (**7**); HIN = isonicotinic acid, HAc = acetic acid] were synthesized and characterized by elemental analyses, IR spectra, UV spectra, thermogravimetric analyses, powder X-ray diffraction, and single-crystal X-ray diffraction. The polyoxoanionic skeletons $\{[Sn(CH_3)W_2O_4(IN)][(B\text{-}\alpha\text{-}TeW_8O_{31})RE(H_2O)\ (Ac)]_2\}_2^{20-}$ of **1**−**7** are constructed from two symmetrical units $\{[Sn(CH_3)W_2O_4(IN)][(B\text{-}\alpha\text{-}TeW_8O_{31})RE(H_2O)\ (Ac)]_2\}^{10-}$ linked by two acetate connectors, which not only represent the first inorganic−organic hybrid RE-substituted tellurotungstates involving three different organic ligands, but also stand for the first samples of organotin−RE heterometallic polyoxometalate derivatives. The solid-state luminescent emission properties of **2**−**5** mainly display the characteristic emission bands of RE^{III} cations, whereas during the emission procedure of **7**, $[B\text{-}\alpha\text{-}TeW_8O_{31}]^{10-}$ segments make a nonignorable contribution to the PL behavior of **7** accompanying by the occurrence of the intramolecular energy transfer from O→W LMCT energy to Tb^{3+} centers. Furthermore, **4@CTAB** composites with peanutlike and honeycombed morphologies were prepared by a surfactant cetyltrimethylammonium bromide (CTAB). The time-resolved emission spectra of the **4@CTAB** composite with CTAB/**4** = 0.033/0.05 consolidate the energy transfer from CTAB to RE^{III} centers. Variable-temperature magnetic susceptibility measurements for **2**, **3**, and **4** were performed.

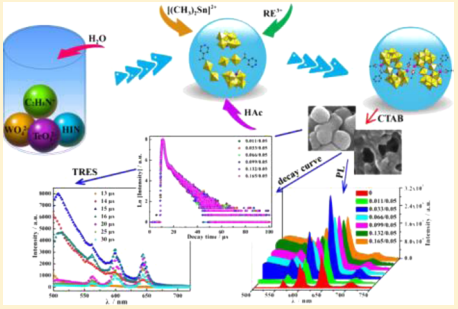

1. INTRODUCTION

The design and fabrication of novel polyoxometalate (POM)-based materials (PBMs) have stimulated considerable interest since the first putative POM was discovered in 1826 because of their extraordinary structural versatility and various potential applications ranging from catalysis, medicine, and magnetism to materials sciences and nanotechnology.[1−9] In the past several decades, PBMs have witnessed great progress in the transition-metal (TM), rare-earth (RE), and organometal derivatives. Furthermore, remarkable results are unremittingly achieved in the large domains of inorganic or organic−inorganic hybrid TM-, RE-, TM−RE-incorporated PBMs as well as a tremendous number of organometal-functionalized PBMs.[10−22]

Although there are several reports on POM-based organometal-TM heterometallic materials recently,[23−28] to the best of our knowledge, no POM-based organometal−RE heterometallic materials have been documented, which is probably related to the fact that the majority of reported organometallic PBMs (such as organosilicon, organophosphorus, organogermanium, etc.) were made in organic solvents,[17] which to a great extent hinders the incorporation of RE ions into the synthetic system. Delightedly, the recent development of organotin groups as excellent candidates for the isolation of organotin-encapsulated PBMs performed in water reagents has made it possible to prepare POM-based organotin−RE heterometallic materials (PBORHMs).[29,30] This background provides us an excellent opportunity and a great possibility to further explore this research realm. Thus, with the aim of creating novel PBORHMs, we launched intensive explorations on the organotin−RE−tellurotungstate system by the one-pot self-assembly strategy in the participation of organic ligands based on the following considerations: (a) organotin groups are water-soluble and the similar sizes of Sn^{IV} to W^{VI} facilitate the direct grafting of organotin fragments into the defect sites of polyoxoanions, particularly, the electrophile $[(CH_3)_2Sn]^{2+}$ group has demonstrated the feasibility in constructing novel structures in the lone-electron-pair-containing heteropolyoxotungstate system;[17,29,30] (b) the lone-electron-pair active trigonal-pyramidal-TeO_3 group can to some extent prevent the formation of closed POM skeletons; meanwhile, the elaborative combination of low-valence Te^{IV} ions with simple tungstates are beneficial to the generation of highly negative charge POM segments in the self-assembly process and thereby

Received: April 10, 2017
Published: June 5, 2017

DOI: 10.1021/acs.inorgchem.7b00924
Inorg. Chem. 2017, 56, 7257−7269

inducing much more RE and $[(CH_3)_2Sn]^{2+}$ electrophiles as linkers to generate polymeric PBORHMs; (c) the synergistic effect of three kinds of organic solubilizers [dimethylamine hydrochloride, acetic acid (HAc), and isonicotinic acid (HIN)] can effectively improve the reactivity of in situ formed tellurotungstate fragments with RE^{3+} cations in aqueous medium;[22] moreover, organic carboxylic acid solubilizers can also serve as the connectors to combine different metal centers together, which favor to give rise to novel inorganic−organic hybrid PBORHMs with intriguing structures and properties. In this article, we report the first class of unseen PBORHMs $[H_2N(CH_3)_2]_6H_{12}Na_2\{[Sn(CH_3)W_2O_4(IN)][(B\text{-}\alpha\text{-}TeW_8O_{31})\text{-}RE(H_2O)(Ac)]_2\}_2\cdot 25H_2O$ {$\mathbf{Sn_2RE_4Te_4W_{36}}$} [RE = Ce^{III} (**1**), Pr^{III} (**2**), Nd^{III} (**3**), Sm^{III} (**4**), Eu^{III} (**5**), Gd^{III} (**6**), Tb^{III} (**7**)] (Scheme S1, Supporting Information), which are characterized by elemental analyses, IR spectra, UV spectra, single-crystal X-ray diffraction (XRD), powder X-ray diffraction (PXRD), and thermogravimetric (TG) analyses. The photoluminescence (PL) properties of **2**−**5** and magnetic properties of **2**, **3**, and **4** were investigated. Moreover, **4@CTAB** (CTAB = cetyltrimethylammonium bromide) composites were prepared, and the peanutlike and honeycombed morphologies of **4@CTAB** composites can be tuned by the usage of CTAB. The PL behaviors of **4** and **4@CTAB** composites were comprehensively probed, revealing that the morphology and the size of composites and the interactions between CTAB and **4** can affect the PL emission. The energy transfer phenomenon from CTAB to RE^{3+} ions in **4@CTAB** composites was verified by the time-resolved emission spectra (TRES) measurements.

2. EXPERIMENTAL SECTION

Materials and Physical Measurements. All chemicals were commercially purchased and used without further purification. C, H, and N elemental analyses were performed on a Perkin−Elmer 2400−II CHNS/O analyzer. Inductively coupled plasma atomic emission spectrometry analyses were measured on a Perkin−Elmer Optima 2000 ICP-AES spectrometer. IR spectra were recorded on a Bruker Vertex 70 IR spectrometer from solid samples palletized with KBr in the range of 4000−450 cm^{-1}. PXRD patterns were collected on a Bruker AXS D8 Advance diffractometer instrument with Cu Kα radiation (λ = 1.540 56 Å) at 293 K. UV spectra were recorded on a Hitachi U-4100 UV−vis−near-IR spectrometer. TG analyses were conducted using a Mettler−Toledo TGA/SDTA 851^e instrument under a flowing N_2 atmosphere with a heating rate of 10 °C min^{-1} from 25 to 1000 °C. PL spectra and excitation-wavelength-dependent PL spectra were recorded on an FLS 980 Edinburgh Analytical Instrument apparatus equipped by a 450 W xenon lamp. PL decay lifetime and time-resolved emission spectra were measured using a μF900H high-energy microsecond flash lamp as the excitation source. Variable-temperature magnetic measurements were conducted on the Quantum Design SQUID magnetometer (MPMS−VSM) in the range of 1.8−300 K. The as-prepared **4@CTAB** composites were characterized by scanning electron microscope (SEM) using JSM−7610F microscope. Samples for SEM measurements were obtained by evaporating a drop of the suspension (precipitate in ethanol) onto a silicon pellet supported by gold spraying.

*$[H_2N(CH_3)_2]_6H_{12}Na_2\{[Sn(CH_3)W_2O_4(IN)][B\text{-}\alpha\text{-}TeW_8O_{31}Ce(H_2O)(Ac)]_2\}_2\cdot 25H_2O$ (**1**).* $Na_2WO_4\cdot 2H_2O$ (2.003 g, 6.060 mmol), K_2TeO_3 (0.201 g, 0.788 mmol), isonicotinic acid (0.150 g, 1.218 mmol), dimethylamine hydrochloride (1.002 g, 12.220 mmol), and 0.5 mL of glacial acetic acid were dissolved in 20 mL of distilled water under stirring. After it was stirred for 10 min, $Ce(NO_3)_3\cdot 6H_2O$ (0.250 g, 0.576 mmol) and $(CH_3)_2SnCl_2$ (0.252 g, 1.140 mmol) were consecutively added to the solution, and the final pH of the solution was kept at 4.5 by 6 mol L^{-1} HCl. This solution was stirred for another 10 min, heated at 90 °C for 2 h, cooled to room temperature, and filtered. The filtrate was left to evaporate slowly for crystallization. Yellow block crystals of **1** were isolated after two weeks. Yield: 0.23 g (14.19% based on $Ce(NO_3)_3\cdot 6H_2O$). Anal. Calcd (%): C, 3.50; H, 1.83; N, 0.96; Na, 0.39; W, 56.65; Ce, 4.80; Sn, 2.03. Found: C, 3.63; H, 1.95; N, 1.03; Na, 0.52; W, 56.78; Ce, 4.61; Sn, 2.18.

*$[H_2N(CH_3)_2]_6H_{12}Na_2\{[Sn(CH_3)W_2O_4(IN)][B\text{-}\alpha\text{-}TeW_8O_{31}Pr(H_2O)(Ac)]_2\}_2\cdot 25H_2O$ (**2**).* The synthesis of **2** is similar to **1** except for $Pr(NO_3)_3\cdot 6H_2O$ (0.250 g, 0.575 mmol) instead of $Ce(NO_3)_3\cdot 6H_2O$. Green block crystals of **2** were obtained. Yield: 0.23 g (14.19% based on $Pr(NO_3)_3\cdot 6H_2O$). Anal. Calcd (%): C, 3.49; H, 1.83; N, 0.96; Na, 0.39; W, 56.64; Pr, 4.82; Sn, 2.03. Found: C, 3.58; H, 1.97; N, 1.12; Na, 0.46; W, 56.80; Pr, 4.70; Sn, 2.20.

*$[H_2N(CH_3)_2]_6H_{12}Na_2\{[Sn(CH_3)W_2O_4(IN)][B\text{-}\alpha\text{-}TeW_8O_{31}Nd(H_2O)(Ac)]_2\}_2\cdot 25H_2O$ (**3**).* The synthesis of **3** is similar to **1** except for $Nd(NO_3)_3\cdot 6H_2O$ (0.250 g, 0.570 mmol) instead of $Ce(NO_3)_3\cdot 6H_2O$. Purple block crystals of **3** were obtained. Yield: 0.22 g (13.58% based on $Nd(NO_3)_3\cdot 6H_2O$). Anal. Calcd (%): C, 3.49; H, 1.83; N, 0.96; Na, 0.39; W, 56.57; Nd, 4.93; Sn, 2.03. Found: C, 3.57; H, 1.94; N, 1.05; Na, 0.51; W, 56.77; Nd, 4.86; Sn, 2.20.

*$[H_2N(CH_3)_2]_6H_{12}Na_2\{[Sn(CH_3)W_2O_4(IN)][B\text{-}\alpha\text{-}TeW_8O_{31}Sm(H_2O)(Ac)]_2\}_2\cdot 25H_2O$ (**4**).* The synthesis of **4** is similar to **1** except for $Sm(NO_3)_3\cdot 6H_2O$ (0.250 g, 0.562 mmol) instead of $Ce(NO_3)_3\cdot 6H_2O$. Light yellow block crystals of **4** were obtained. Yield: 0.21 g (12.96% based on $Sm(NO_3)_3\cdot 6H_2O$). Anal. Calcd (%): C, 3.48; H, 1.82; N, 0.96; Na, 0.39; W, 56.45; Sm, 5.13; Sn, 2.03. Found: C, 3.61; H, 1.98; N, 1.11; Na, 0.47; W, 56.58; Sm, 4.97; Sn, 2.17.

*$[H_2N(CH_3)_2]_6H_{12}Na_2\{[Sn(CH_3)W_2O_4(IN)][B\text{-}\alpha\text{-}TeW_8O_{31}Eu(H_2O)(Ac)]_2\}_2\cdot 25H_2O$ (**5**).* The synthesis of **5** is similar to **1** except for $Eu(NO_3)_3\cdot 6H_2O$ (0.250 g, 0.560 mmol) instead of $Ce(NO_3)_3\cdot 6H_2O$. Colorless block crystals of **5** were obtained. Yield: 0.21 g (12.96% based on $Eu(NO_3)_3\cdot 6H_2O$). Anal. Calcd (%): C, 3.48; H, 1.82; N, 0.96; Na, 0.39; W, 56.42; Eu, 5.18; Sn, 2.02. Found: C, 3.62; H, 1.92; N, 1.05; Na, 0.49; W, 56.55; Eu, 5.01; Sn, 2.14.

*$[H_2N(CH_3)_2]_6H_{12}Na_2\{[Sn(CH_3)W_2O_4(IN)][B\text{-}\alpha\text{-}TeW_8O_{31}Gd(H_2O)(Ac)]_2\}_2\cdot 25H_2O$ (**6**).* The synthesis of **6** is similar to **1** except for $Gd(NO_3)_3\cdot 6H_2O$ (0.250 g, 0.554 mmol) instead of $Ce(NO_3)_3\cdot 6H_2O$. Colorless block crystals of **6** were obtained. Yield: 0.19 g (11.73%) based on $Dy(NO_3)_3\cdot 6H_2O$. Anal. Calcd (%): C, 3.47; H, 1.82; N, 0.95; Na, 0.39; W, 56.32; Gd, 5.35; Sn, 2.02. Found: C, 3.58; H, 2.01; N, 1.00; Na, 0.42; W, 56.41; Gd, 5.29; Sn, 2.18.

*$[H_2N(CH_3)_2]_6H_{12}Na_2\{[Sn(CH_3)W_2O_4(IN)][B\text{-}\alpha\text{-}TeW_8O_{31}Tb(H_2O)(Ac)]_2\}_2\cdot 25H_2O$ (**7**).* The synthesis of **7** is similar to **1** except for $Tb(NO_3)_3\cdot 6H_2O$ (0.250 g, 0.552 mmol) instead of $Ce(NO_3)_3\cdot 6H_2O$. Colorless block crystals of **7** were obtained. Yield: 0.17 g (10.55%) based on $Tb(NO_3)_3\cdot 6H_2O$. Anal. Calcd (%): C, 3.47; H, 1.82; N, 0.95; Na, 0.39; W, 56.29; Tb, 5.41; Sn, 2.02. Found: C, 3.65; H, 1.96; N, 1.07; Na, 0.45; W, 56.37; Tb, 5.36; Sn, 2.13.

Preparations of Various 4@CTAB Composites. A solution of 0.050 g of presynthesized **4** dissolving in 5 mL of distilled water was added to the solution of 5 mL of ethanol containing 0.011 g of CTAB under ultrasonic stirring. A resulting turbid suspension was centrifugally separated, and the precipitate was collected, washed with ethanol three times, and dried in the oven at 40 °C for 1 h. Similarly, other **4@CTAB** composites can be obtained by 0.033, 0.066, 0.099, 0.132, or 0.165 g of CTAB instead of 0.011 g CTAB.

X-ray Crystallography. High-quality crystals of **1**−**7** were picked from their mother liquors and sealed in a capillary tube for data collection. Their intensity data were collected on a Bruker Apex II diffractometer equipped with a CCD bidimensional detector with the graphite-monochromated Mo Kα radiation (λ = 0.710 73 Å) at 296(2) K. Data reduction was executed by the SAINT software suite.[31] The absorption correction was based on multiple and symmetry-equivalent reflections in the data set using the SADABS program.[32] These structures were determined by direct methods and refined by means of full-matrix least-squares on F^2 using the SHELXTL-97 program package.[33,34] All non-hydrogen atoms were refined anisotropically except for some oxygen, nitrogen, and carbon atoms and water molecules. All hydrogen atoms associated with carbon and nitrogen atoms were geometrically placed and isotropically refined using a riding mode by the default SHELXTL parameters. All non-hydrogen

DOI: 10.1021/acs.inorgchem.7b00924
Inorg. Chem. 2017, 56, 7257−7269

Table 1. Crystallographic Data and Structure Refinements for 1−7

	1	2	3	4	5	6	7
empirical formula	$C_{34}H_{212}N_8Na_2Ce_4O_{186}Sn_2Te_4W_{36}$	$C_{34}H_{212}N_8Na_2Pr_4O_{186}Sn_2Te_4W_{36}$	$C_{34}H_{212}N_8Na_2Nd_4O_{186}Sn_2Te_4W_{36}$	$C_{34}H_{212}N_8Na_2Sm_4O_{186}Sn_2Te_4W_{36}$	$C_{34}H_{212}N_8Na_2Eu_4O_{186}Sn_2Te_4W_{36}$	$C_{34}H_{212}N_8Na_2Gd_4O_{186}Sn_2Te_4W_{36}$	$C_{34}H_{212}N_8Na_2Tb_4O_{186}Sn_2Te_4W_{36}$
formula weight	11 682.96	11 686.12	11 699.44	11 723.88	11 730.32	11 751.48	11 758.16
crystal system	triclinic	triclinic	triclinic	triclinic	triclinic	triclinic	triclinic
space group	$P\bar{1}$	$P\bar{1}$	$P\bar{1}$	$P\bar{1}$	$P\bar{1}$	$P\bar{1}$	$P\bar{1}$
a, Å	17.029(3)	16.9778(10)	16.1971(13)	16.870(3)	16.309(2)	16.787(7)	16.2550(15)
b, Å	17.247(4)	17.1999(10)	16.9881(14)	17.071(3)	17.110(2)	16.931(8)	17.0799(15)
c, Å	22.206(5)	22.1813(12)	22.1861(19)	22.038(3)	22.554(3)	21.960(10)	22.4827(19)
α, deg	88.776(4)	88.6420(10)	89.034(2)	88.686(3)	89.715(2)	88.742(8)	89.894(2)
β, deg	75.104(4)	75.1190(10)	75.0250(10)	74.699(3)	73.886(2)	74.383(8)	73.854(2)
γ, deg	74.117(4)	74.5500(10)	74.1530(10)	73.972(3)	75.547(2)	74.056(8)	75.421(2)
V, Å^{-3}	6054(2)	6026.9(6)	5663.7(8)	5875.2(19)	5839.4(12)	5771(4)	5776.4(9)
Z	1	1	1	1	1	1	1
μ, mm^{-1}	18.531	18.667	19.920	19.319	19.506	19.801	19.857
$F(000)$	5186	5190	5194	5202	5206	5210	5214
T, K	296(2)	296(2)	296(2)	296(2)	296(2)	296(2)	296(2)
limiting indices	$-18 \le h \le 20$	$-20 \le h \le 15$	$-19 \le h \le 14$	$-13 \le h \le 20$	$-19 \le h \le 13$	$-19 \le h \le 13$	$-18 \le h \le 19$
	$-20 \le k \le 19$	$-19 \le k \le 20$	$-20 \le k \le 14$	$-20 \le k \le 20$	$-19 \le k \le 20$	$-20 \le k \le 19$	$-18 \le k \le 20$
	$-26 \le l \le 26$	$-26 \le l \le 26$	$-26 \le l \le 26$	$-25 \le l \le 26$	$-26 \le l \le 26$	$-26 \le l \le 25$	$-26 \le l \le 19$
No.of reflections collected	30 377	31 219	28 611	29 236	27 743	29 728	29 240
No.of independent reflections	20 785	21 117	19 676	20 425	19 552	20 114	20 134
R_{int}	0.0634	0.0457	0.0642	0.0580	0.0658	0.0533	0.0748
GOF on F^2	1.017	1.031	1.024	1.029	1.004	1.012	1.021
final R indices [$I > 2\sigma(I)$]	$R_1 = 0.0908$	$R_1 = 0.0585$	$R_1 = 0.0733$	$R_1 = 0.0977$	$R_1 = 0.0960$	$R_1 = 0.0616$	$R_1 = 0.0825$
	$wR_2 = 0.2261$	$wR_2 = 0.1533$	$wR_2 = 0.1810$	$wR_2 = 0.2587$	$wR_2 = 0.2340$	$wR_2 = 0.1449$	$wR_2 = 0.1958$
R indices (all data)	$R_1 = 0.1513$	$R_1 = 0.1087$	$R_1 = 0.1013$	$R_1 = 0.1323$	$R_1 = 0.1697$	$R_1 = 0.1037$	$R_1 = 0.1333$
	$wR_2 = 0.2517$	$wR_2 = 0.1868$	$wR_2 = 0.1959$	$wR_2 = 0.2828$	$wR_2 = 0.2686$	$wR_2 = 0.1586$	$wR_2 = 0.2173$

DOI: 10.1021/acs.inorgchem.7b00924
Inorg. Chem. 2017, 56, 7257−7269

atoms except for oxygen, carbon, and nitrogen atoms and water molecules were anisotropically refined. No hydrogen atoms attached to water molecules were located from the difference Fourier map. For **1**−**7**, there are still solvent-accessible voids in the check cif reports of crystal structures, suggesting that some water molecules should exist in the structures that cannot be found from the weak residual electron peaks. These water molecules are highly disordered, and attempts to locate and refine them were unsuccessful. On the basis of elemental analyses and TG analyses, another 13 water molecules were directly added to the molecular formula. Crystal data and structure refinements for **1**−**7** are listed in Table 1.

3. RESULTS AND DISCUSSION

Structural Description. The experimental PXRD patterns for **1**−**7** are well consistent with the simulated XRD patterns from the single-crystal diffraction data, demonstrating the high phase purity of the samples used for the property measurements (Figure S1, Supporting Information). Bond valence sum (BVS) calculations reveal that the chemical valences of all RE, Te, and W atoms are +3, +3, and +6, respectively (Table S1, Supporting Information).

1−**7** are isomorphous and crystallize in the triclinic space group $P\bar{1}$, representing the first inorganic−organic hybrid organotin−RE heterometallic tellurotungstates;[35,36] thus, only the structure of **3** is described. Structural analysis reveals that **3** displays a unique tetrameric polyoxoanionic skeleton $\{[Sn(CH_3)W_2O_4(IN)][(B\text{-}\alpha\text{-}TeW_8O_{31})Nd(H_2O)(Ac)]_2\}_2^{20-}$ (Figure 1a) that is assembled from two symmetrical units $\{[Sn(CH_3)W_2O_4(IN)][(B\text{-}\alpha\text{-}TeW_8O_{31})Nd(H_2O)(Ac)]_2\}^{10-}$ **{SnNd$_2$Te$_2$W$_{18}$}** (Figure 1b) linked by two Ac^- connectors (Figure S2, Supporting Information). The dimeric **{SnNd$_2$Te$_2$W$_{18}$}** unit consists of a $[(B\text{-}\alpha\text{-}TeW_8O_{31})_2W_2O_4(IN)]^{17-}$ moiety (Figure 1c) made of two rare tetravacant $[B\text{-}\alpha\text{-}TeW_8O_{31}]^{10-}$ subunits (Figure 2a) sandwiching a vertex-

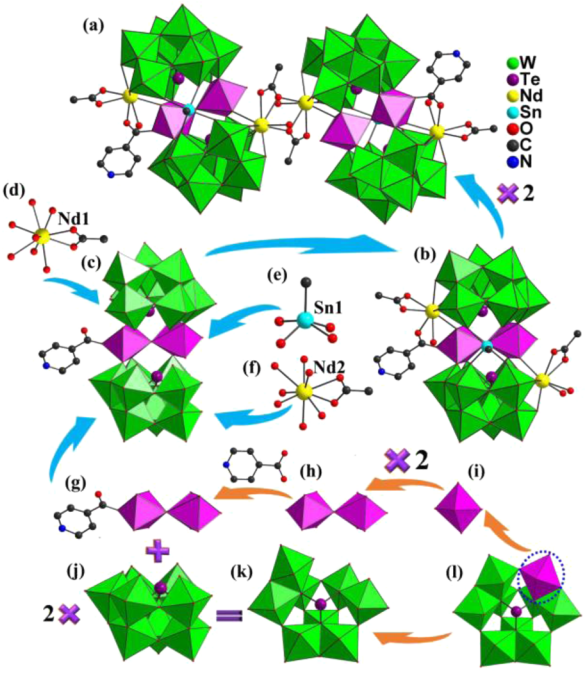

Figure 1. (a) The tetrameric skeleton of **3**. (b) The symmetric dimeric unit of **3**. (c) The $[(B\text{-}\alpha\text{-}TeW_8O_{31})_2W_2O_4(IN)]^{17-}$ fragment. (d, f) Coordination modes of $Nd1^{3+}$ and $Nd2^{3+}$ cations. (e) The demethylated $[Sn(CH_3)]^{3+}$ group. (g−i) The $[W_2O_4(IN)]^{3+}$ segment formed by two vertex-sharing $\{WO_6\}$ units and an IN^- ligand. (j, k) The rare $[B\text{-}\alpha\text{-}TeW_8O_{31}]^{10-}$ subunit. (l) The common $[B\text{-}\alpha\text{-}TeW_9O_{33}]^{8-}$ building unit.

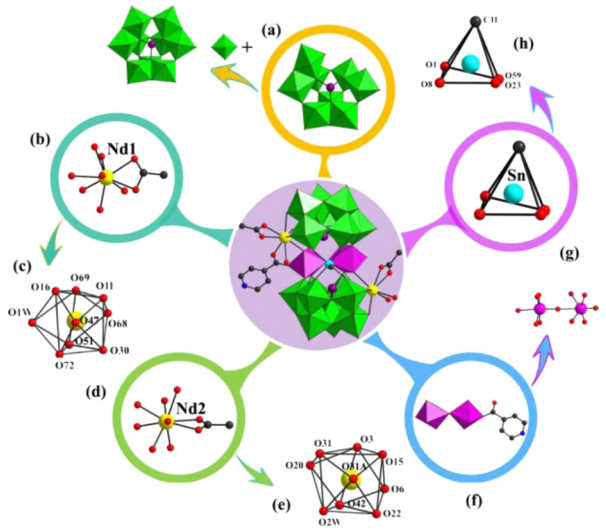

Figure 2. (a) The $[B\text{-}\alpha\text{-}TeW_8O_{31}]^{10-}$ unit formed by the removal of one $\{WO_6\}$ octahedron from the common $[B\text{-}\alpha\text{-}TeW_9O_{33}]^{8-}$ building block. (b, c) The $\{Nd1(H_2O)(Ac)\}$ moiety and the nonacoordinate severely distorted tricapped triangular prism geometry of $Nd1^{3+}$ cation defined by four O atoms deriving from one $[B\text{-}\alpha\text{-}TeW_8O_{31}]^{10-}$ fragment, one O atom from the $[W_2O_4(IN)]^{3+}$ segment, one O atom from a terminal water molecule, one carboxyl O atom of an IN^- ligand and two carboxyl O atoms from one Ac^- ligand. (d, e) The $\{Nd2(H_2O)(Ac)\}$ moiety and the nonacoordinate severely distorted tricapped triangular prism geometry of $Nd2^{3+}$ ion defined by four O atoms deriving from one $[B\text{-}\alpha\text{-}TeW_8O_{31}]^{10-}$ fragment, one O atom from the $[W_2O_4(IN)]^{3+}$ segment, one O atom from a terminal water molecule, and three carboxyl O atoms from two Ac^- ligands. (f) The IN^--decorated metal−organic $[W_2O_4(IN)]^{3+}$ unit. (g) The $[Sn(CH_3)]^{3+}$ group and the coordination geometry of the Sn^{4+} cation. Symmetry codes: A: $-x$, $1-y$, $1-z$.

sharing IN-decorated $[W_2O_4(IN)]^{3+}$ group, a functionalized $[Sn(CH_3)]^{3+}$ group, a supporting $\{Nd(H_2O)(Ac)\}^{2+}$ segment, and a bridging $\{Nd(H_2O)(Ac)\}^{2+}$ cation (Figure 1d−g). In **{SnNd$_2$Te$_2$W$_{18}$}**, two crystallographically independent Nd^{3+} ions ($Nd1^{3+}$ and $Nd2^{3+}$) (Figure 1d,f) embedded in the vacant sites of the tetralacunary $[B\text{-}\alpha\text{-}TeW_8O_{31}]^{10-}$ moieties reveal the nonacoordinate severely distorted tricapped trigonal prism geometries defined by four O atoms from a $[B\text{-}\alpha\text{-}TeW_8O_{31}]^{10-}$ fragment, one O atom from the $[W_2O_4(IN)]^{3+}$ segment, one O atom from a terminal water molecule and three carboxyl O atoms from one IN^- ligand and one Ac^- ligand for the $Nd1^{3+}$ ion, and three carboxyl O atoms from one IN^- ligand and one Ac^- ligand for the $Nd1^{3+}$ ion, and three carboxyl O atoms from Ac^- ligands for the $Nd2^{3+}$ ion (Figure 2b−e). It is worth noting that during the preparation of **3**, the initial material $[Sn(CH_3)_2]^{2+}$ undergoes a demethylated structural conversion into the $[Sn(CH_3)]^{3+}$ group (Figure 1e) for the sake of reducing steric hindrance and enhancing cohesion of the structure as it subtly accommodates the insertion between two $[B\text{-}\alpha\text{-}TeW_8O_{31}]^{10-}$ subunits by coordinating to O atoms from the equatorial belt W centers via four Sn−O bonds and exhibits a peculiar pentacoordinate square pyramid configuration (Figure 2g−h), which is first observed in the organotin-based POM chemistry. The ditungsten metal−organic unit $[W_2O_4(IN)]^{3+}$ (Figure 1g) located in the central belt of the **{SnNd$_2$Te$_2$W$_{18}$}** unit encompasses two parallel distributed W atoms linked via a

DOI: 10.1021/acs.inorgchem.7b00924
Inorg. Chem. 2017, 56, 7257−7269

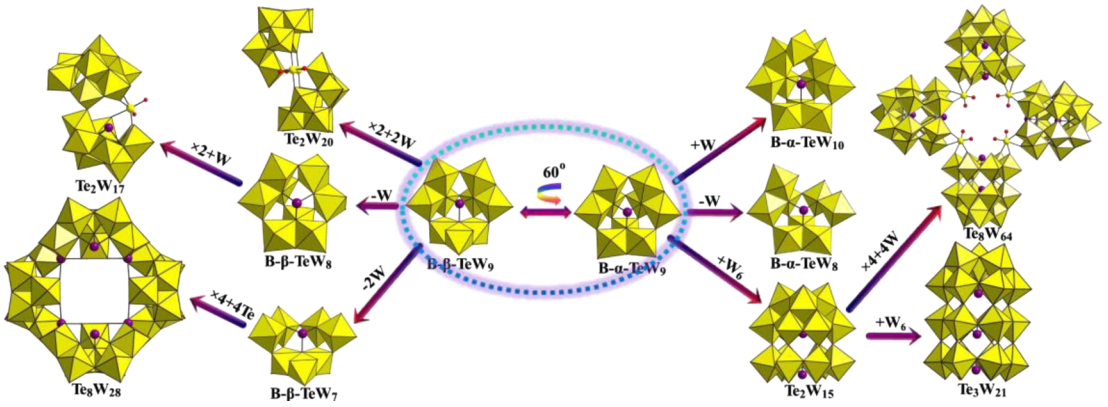

Figure 3. Various tellurotungstate building blocks observed in reported Te^{IV}-containing lacunary polytungstates.

vertex-sharing O atom, and one of the W atoms is directly bonded to a decorated IN^- ligand (Figure 1h,i and Figure 2f), which at the same time, is grafted to a $[Nd(H_2O)\ (Ac)]^{2+}$ ornament (Figure S3, Supporting Information). In other words, two carboxyl O atoms deriving from the IN^- ligand are synchronously captured by the $\{W_2O_4\}$ group and one coordination sphere of $Nd1^{3+}$ cation. Notably, the coordination of IN^- ligand to both W and RE centers by means of carboxyl O atoms is rare within a POM, while coordination to either of them is common.[37−44] Although various tellurotungstate polyoxoanion fragments have been obtained through the one-pot self-assembly strategy (Figure 3),[45−53] the unusual $[B\text{-}\alpha\text{-}TeW_8O_{31}]^{10-}$ (Figure 1j,k) unit that can be reasonably described as the cleavage of a single W center from the common $[B\text{-}\alpha\text{-}TeW_9O_{33}]^{8-}$ (Figure 1l) building block was not reported previously, which is structurally related to the $[B\text{-}\alpha\text{-}SbW_8O_{31}]^{11-}$ unit first reported in $[\{RE(H_2O)\}\{RE(pic)\}(Sb_3O_4)(B\text{-}\alpha\text{-}SbW_8O_{31})(B\text{-}\alpha\text{-}SbW_{10}O_{35})]_2^{24-}$ (RE = Tb^{III}, Dy^{III}, Ho^{III}; pic = picolinic acid).[37] Thus, it can be drawn a summary that two $[B\text{-}\alpha\text{-}TeW_8O_{31}]^{10-}$ units incorporating two $[Nd(H_2O)\ (Ac)]^{2+}$ fragments into the vacant sites are fused together by a metal−organic $[W_2O_4(IN)]^{3+}$ segment and a demethylated $[Sn(CH_3)]^{3+}$ group giving rise to an intriguing inorganic−organic hybrid dimer $\{\mathbf{SnNd_2Te_2W_{18}}\}$, in which the $\{Nd(H_2O)\ (Ac)\}^{2+}$ fragment works as the bridge via the Ac^- ligand in a μ_3-O connection motif to link two symmetrical dimeric units, generating a fantastic tetrameric aggregate $\{\mathbf{Sn_2Nd_4Te_4W_{36}}\}$. Some remarkable features should be noted in **1**−**7**: (i) $\{\mathbf{Sn_2RE_4Te_4W_{36}}\}$ illustrates the first case of inorganic−organic hybrid RE-containing tellurotungstates; (ii) $\{\mathbf{Sn_2RE_4Te_4W_{36}}\}$ is the only one example of RE-substituted POMs involving three distinct organic ligands by far; (iii) $\{\mathbf{Sn_2RE_4Te_4W_{36}}\}$ sets a precedent for a new territory of PBORHMs. In addition, discrete $\{\{\mathbf{Sn_2RE_4Te_4W_{36}}\}$ polyoxoanions are regularly distributed in the −AAA− mode along the *b* and *c* axes (Figure 4), and the three-dimensional (3D) supramolecular structure is built by the H-bonding interactions (Figure S4, Supporting Information).

IR Spectra. The structural characteristics of **1**−**7** are further ascertained by IR spectra from solid samples palletized with KBr in the range of 4000−450 cm^{-1} (Figure S5, Supporting Information). It is easy to discover that all the IR spectra possess similar vibration patterns, demonstrating that **1**−**7** have the same basic structural frameworks, which are well consistent with the results of single-crystal X-ray analyses. In the low wavenumber (ν < 1000 cm^{-1}) region, several characteristic

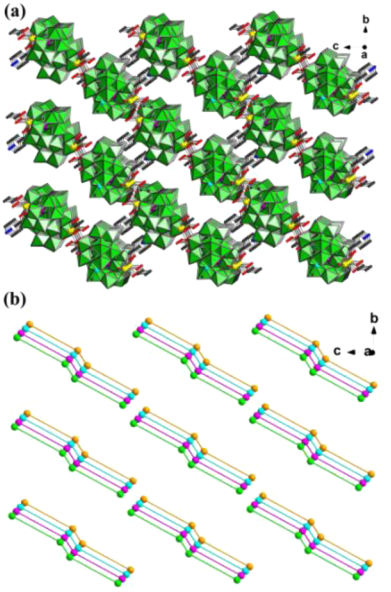

Figure 4. (a) The 3D stacking mode of **3** along *a*-axis. (b) The simplified 3D stacking mode of **3** along *a*-axis.

vibrations appearing at 953, 881, 813, and 673 cm^{-1} for **1**, 954, 882, 817, and 667 cm^{-1} for **2**, 955, 884, 816, and 673 cm^{-1} for **3**, 953, 883, and 667 cm^{-1} for **4**, 956, 883, 820, and 673 cm^{-1} for **5**, 956, 880, 793, and 656 cm^{-1} for **6**, and 956, 880, 791, and 650 cm^{-1} for **7** are, respectively, ascribed to the $\nu(W{-}O_t)$, $\nu(W{-}O_b)$, and $\nu(W{-}O_c)$ vibrations derived from the tetravacant Keggin $[B\text{-}\alpha\text{-}TeW_8O_{31}]^{10-}$ fragments. The peak at 704 cm^{-1} for **1**, 705 cm^{-1} for **2**, 704 cm^{-1} for **3**, 703 cm^{-1} for **4**, 704 cm^{-1} for **5**, 700 cm^{-1} for **6**, and 698 cm^{-1} for **7** can be identified as $\nu(Te{-}O)$ vibrations based on the IR spectrum of K_2TeO_3 showing a strong band around 700 cm^{-1}. Apparent shifts are observed in **1**−**7** in comparison with the polyoxoanion $[Te_2W_{17}O_{61}]^{12-}$ [946, 855, 766, 689, and 643 cm^{-1}] that consists of two $[B\text{-}\beta\text{-}TeW_8O_{31}]^{10-}$ building blocks linked by a $\{WO_2\}$ group,[47] which may result from the configuration transformation from $[B\text{-}\beta\text{-}TeW_8O_{31}]^{10-}$ to $[B\text{-}\alpha\text{-}TeW_8O_{31}]^{10-}$ as well as the implanting of the metal−organic moiety $\{W_2O_4(HIN)\}^{4+}$ and $\{Nd(H_2O)\ (Ac)\}^{2+}$ segments into the defects of $[B\text{-}\alpha\text{-}TeW_8O_{31}]^{10-}$ skeletons. In the high wavenumber (ν > 1000 cm^{-1}) region, the weak peak at 1196 cm^{-1} for **1**, 1196 cm^{-1} for **2**, 1195 cm^{-1} for **3**, 1194 cm^{-1} for **4**, 1196 cm^{-1} for **5**, 1194 cm^{-1} for **6**, and 1195 cm^{-1} for **7** is assigned to the $\delta_s(CH_3)$ vibration in methyltin derivatives,

DOI: 10.1021/acs.inorgchem.7b00924
Inorg. Chem. 2017, 56, 7257−7269

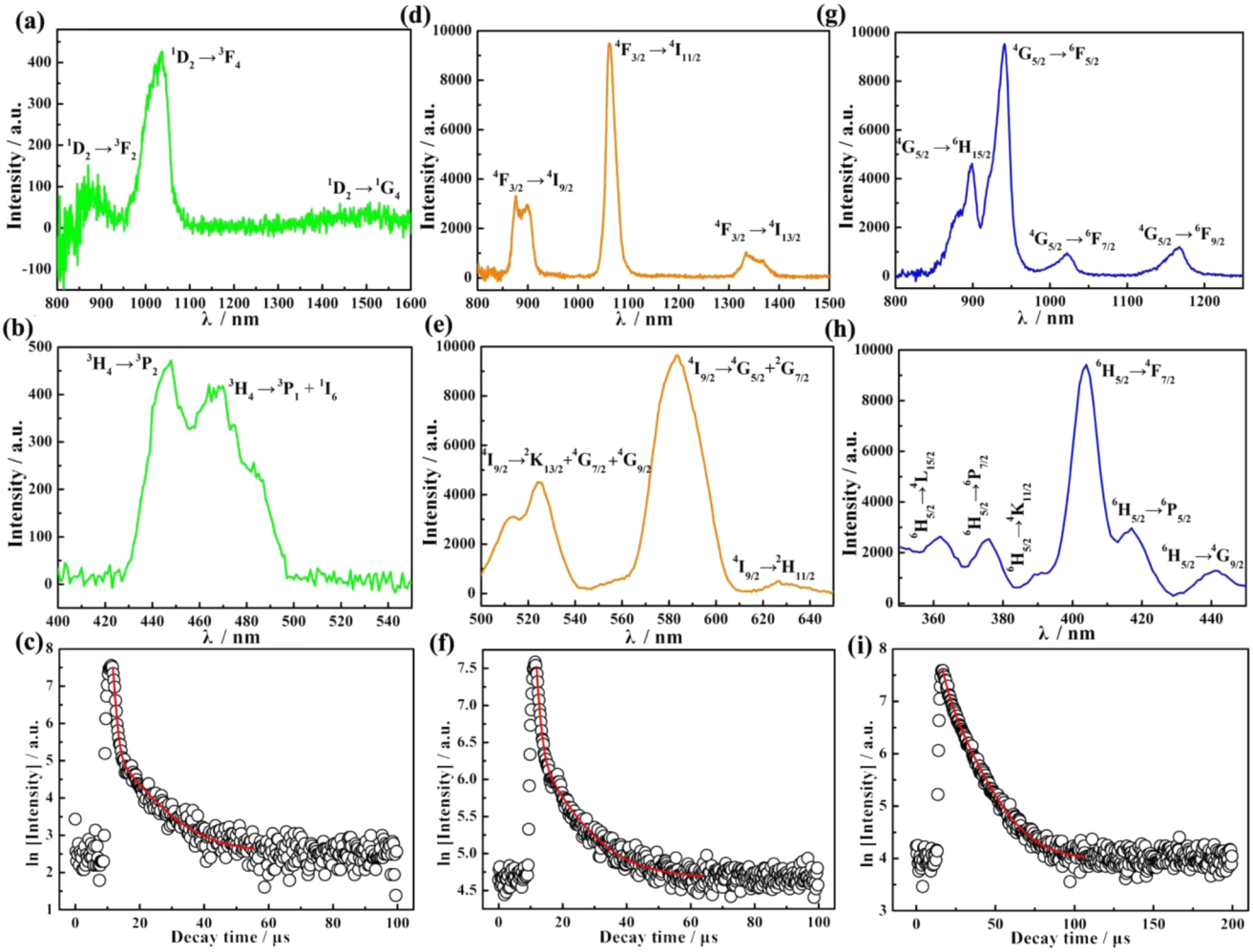

Figure 5. (a) The solid-state NIR emission spectrum of **2** (λ_{ex} = 447 nm) at room temperature. (b) The solid-state excitation spectrum of **2** (λ_{em} = 1035 nm) at room temperature. (c) The luminescence decay curve of **2** by monitoring the emission at 1035 nm. (d) The solid-state NIR emission spectrum of **3** (λ_{ex} = 583 nm) at room temperature. (e) The solid-state excitation spectrum of **3** (λ_{em} = 1062 nm) at room temperature. (f) The luminescence decay curve of **3** by monitoring the emission at 1062 nm. (g) The solid-state emission NIR spectrum of **4** (λ_{ex} = 404 nm) at room temperature. (h) The solid-state excitation spectrum of **4** (λ_{em} = 941 nm) at room temperature. (i) The luminescence decay curve of **4** by monitoring the emission at 941 nm.

which is in good accordance with the previously reported methyltin-functionalized POMs.[53,54] The peaks at 3113−3150 cm^{-1} are ascribed to the N−H stretching vibrations, and the signals at 2793−2799 cm^{-1} are assigned as the C−H stretching vibrations, illustrating the presence of monprotonated dimethylamine cations. Furthermore, the resonances at 1625−1630 cm^{-1} and 1399−1406 cm^{-1} are, respectively, assigned to the asymmetric stretching vibration (ν_{as}) and symmetric stretching vibration (ν_s) of carboxylate (CO_2^-) groups. Generally speaking, the interval [$\Delta\nu = \nu_{as}(CO_2^-) - \nu_s(CO_2^-)$] between $\nu_{as}(CO_2^-) - \nu_s(CO_2^-)$ provides a credible way to judge the coordination mode of CO_2^- groups.[55,56] Thus, in **1**−**7**, the $\Delta\nu$ of 224−226 cm^{-1} indicates the CO_2^- groups mainly adopt bridging fashions in the structures. Besides, the broad vibration bands situated in the range of 3499−3438 cm^{-1} are response for the existence of water molecules. However, the RE−O stretching vibrations of **1**−**7** are absent in the IR scope, which may be in relation to the prominent ionic interactions between the tetravacant [B-α-TeW_8O_{31}]$^{10-}$ segments and RE^{3+} cations.[57,58]

Photoluminescence (PL) Properties. The solid-state near-infrared (NIR) PL properties of **2**, **3**, and **4** and visible PL properties of **4**, **5**, and **7** were studied at room temperature (Figures 5 and 6 and Figure S6, Supporting Information). In contrast to other RE^{3+} ions, Pr^{3+} ions are of particular interest and versatile, since they can exhibit emission lines from three different levels ($^3P_0$, $^1D_2$, and $^1G_4$) under excitation, thereby producing a more complicated luminescent behavior.[59] Generally, transitions from the $^1D_2$ level are more likely than those from the $^3P_0$ level on account that radiative transitions are more prone to occur under the condition of larger energy gaps.[60] Upon excitation at 447 nm, the NIR emission spectrum of **2** shows three typical emission bands at 869, 1035, and 1498 nm, which can be assigned to the $^1D_2 \rightarrow {}^3F_2$, $^1D_2 \rightarrow {}^3F_4$, and $^1D_2 \rightarrow {}^1G_4$ transitions of Pr^{3+} ions, respectively (Figure 5a).[56] By detecting the strongest $^1D_2 \rightarrow {}^3F_4$ transition, the excitation spectrum of **2** was collected, and two excitation bands located at 447 and 470 nm were clearly observed, attributable to the $^3H_4 \rightarrow {}^3P_2$ and $^3H_4 \rightarrow {}^3P_1 + {}^1I_6$ transitions of the Pr^{3+} ions (Figure 5b).[61] Besides, the luminescence decay curve obtained by monitoring the $^1D_2 \rightarrow {}^3F_4$ emission at 1053 nm (Figure 5c) can be fitted to a second-order exponential function as $I = A_1 \exp(-t/\tau_1) + A_2 \exp(-t/\tau_2)$ (τ_1 and τ_2 are the fast and slow

DOI: 10.1021/acs.inorgchem.7b00924
Inorg. Chem. 2017, 56, 7257−7269

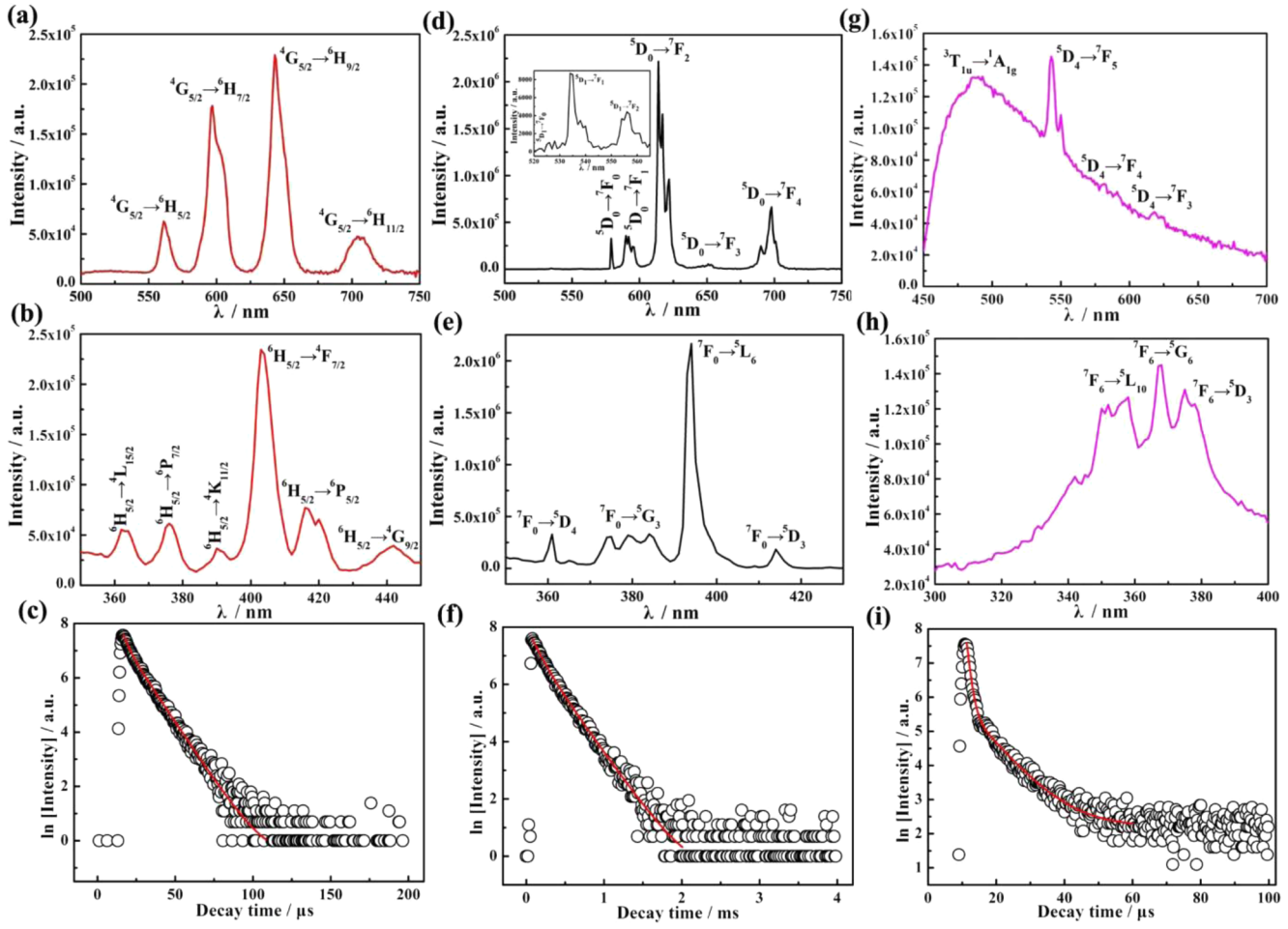

Figure 6. (a) The solid-state emission spectrum of **4** (λ_{ex} = 404 nm) at room temperature. (b) The solid-state excitation spectrum of **4** (λ_{em} = 644 nm) at room temperature. (c) The luminescence decay curve of **4** by monitoring the emission at 644 nm. (d) The solid-state emission spectrum of **5** (λ_{ex} = 395 nm) at room temperature. (e) The solid-state excitation spectrum of **5** (λ_{em} = 615 nm) at room temperature. (f) The luminescence decay curve of **5** by monitoring the emission at 614 nm. (g) The solid-state emission spectrum of **7** (λ_{ex} = 367 nm) at room temperature. (h) The solid-state excitation spectrum of **7** (λ_{em} = 543 nm) at room temperature. (i) The luminescence decay curve of **7** by monitoring the emission at 543 nm.

components of the luminescence lifetimes; A_1 and A_2 are the pre-exponential factors), affording lifetimes of τ_1 = 0.73 μs (45.88%) and τ_2 = 8.76 μs (54.12%). The average lifetime of **2** is determined by the given formula $\tau = (A_1\tau_1^2 + A_2\tau_2^2)/(A_1\tau_1 + A_2\tau_2)$,[62] providing the average lifetime of **2** to be 5.07 μs (Table S2, Supporting Information). The NIR emission spectrum of **3** under the excitation at 583 nm (Figure 5d) exhibits three characteristic emission bands at 898, 1062, and 1333 nm, corresponding to the $^4F_{3/2}\rightarrow{}^4I_{9/2}$, $^4F_{3/2}\rightarrow{}^4I_{11/2}$, and $^4F_{3/2}\rightarrow{}^4I_{13/2}$ transitions of Nd^{3+} ions.[63−65] Among the three emission bands, the strongest emission residing in 1062 nm has latent applications in the laser system, while the band at 1333 nm of the material is suitable for developing optical amplifiers operating at ∼1.3 μm, which offer the great opportunity for application in optical telecommunication.[65] As a result of the multiplicity of excited 4f states in the visible range, some transitions to different states are not resolved, thus usually leading to the relatively broad bands in the excitation of Nd^{3+} ions. Here, several excitation bands appearing at 524, 583, and 626 nm are discerned by monitoring at $^4F_{3/2}\rightarrow{}^4I_{11/2}$ transition at 1062 nm for **3**, which are ascribed to the $^4I_{9/2}\rightarrow{}^2K_{13/2}$ + $^4G_{7/2}$ + $^4G_{9/2}$, $^4I_{9/2}\rightarrow{}^4G_{5/2}$ + $^2G_{7/2}$ and $^4I_{9/2}\rightarrow{}^2H_{11/2}$ transitions of the Nd^{3+} ions (Figure 5e).[64] The lifetime decay profile of **3** (Figure 5f) performed under the most intense emission at 1062 nm and the excitation at 583 nm also abides by a double exponential function, generating τ_1 and τ_2 of 1.05 μs (22.48%) and 10.41 μs (77.52%) and the average lifetime of 8.31 μs. The excitation wavelength of **4** is set at 404 nm, and the NIR spectrum reveals four groups of typical peaks at 899, 941, 1022, and 1168 nm derived from the $^4G_{5/2}\rightarrow{}^6H_{15/2}$, $^4G_{5/2}\rightarrow{}^6F_{5/2}$, $^4G_{5/2}\rightarrow{}^6F_{7/2}$, and $^4G_{5/2}\rightarrow{}^6F_{9/2}$ transitions, and the strongest transition is situated at 941 nm ($^4G_{5/2}\rightarrow{}^6F_{5/2}$; Figure 5g).[66−68] The excitation spectrum of **4** (Figure 5h) obtained by monitoring at 941 nm is composed of several broad emission bands centered at 362, 376, 389, 404, 417, and 441 nm in the UV−visible range. These bands are attributed to the $^6H_{5/2}\rightarrow{}^4L_{15/2}$, $^6H_{5/2}\rightarrow{}^6P_{7/2}$, $^6H_{5/2}\rightarrow{}^4K_{11/2}$, $^6H_{5/2}\rightarrow{}^4F_{7/2}$, $^6H_{5/2}\rightarrow{}^6P_{5/2}$, and $^6H_{5/2}\rightarrow{}^6G_{9/2}$ transitions of the Sm^{III} ions. The lifetime decay curve of **4** (Figure 5i) can be well-fitted by a double exponential function with the lifetimes τ_1 and τ_2 of 4.01 μs (13.31%) and 14.66 μs (86.69%) and the average lifetime of 13.23 μs.

The solid-state visible emission spectrum of **2** upon 470 nm excitation exhibits five peaks at 529, 615, 646, 682, and 729 nm at ambient temperature, which are, respectively, attributed to the $^3P_1\rightarrow{}^3H_5$, $^3P_0\rightarrow{}^3H_6$, $^3P_0\rightarrow{}^3F_2$, $^3P_1\rightarrow{}^3F_2$, and $^3P_0\rightarrow{}^3F_3$ transitions of Pr^{3+} ions (Figure S6a, Supporting Information), and the strongest emission peak is located at 646 nm, which is

DOI: 10.1021/acs.inorgchem.7b00924
Inorg. Chem. 2017, 56, 7257−7269

responsible for the red luminescence. The excitation spectrum obtained by detecting the emission at 646 nm appears one prominent strong band at 470 nm ($^3H_4 \rightarrow {}^3P_1$; Figure S6b, Supporting Information). Furthermore, the lifetime decay curve of **2** was obtained by monitoring the emission at 646 nm, which conforms to the biexponential function, producing lifetimes of τ_1 = 1.97 μs (43.14%) and τ_2 = 11.09 μs (56.86%), and the average lifetime of **2** is 7.13 μs (Figure S6c, Supporting Information). Under excitation at 404 nm, the visible emission spectrum of **4** displays four obvious peaks of emission bands from 500 to 750 nm due to the intra-$^4f_6$ $^4G_{5/2} \rightarrow {}^6H_J$ (J = 5/2, 7/2, 9/2, and 11/2) transitions. Four characteristic emission peaks respectively appear at 561, 596, 644, and 703 nm, corresponding to the $^4G_{5/2} \rightarrow {}^6H_{5/2}$, $^4G_{5/2} \rightarrow {}^6H_{7/2}$, $^4G_{5/2} \rightarrow {}^6H_{9/2}$, and $^4G_{5/2} \rightarrow {}^6H_{11/2}$ transitions (Figure 6a). In general, the magnetic dipole $^4G_{5/2} \rightarrow {}^6H_{5/2}$ emission intensity is insensitive to the symmetry of the local environment of the Sm^{III} ion, whereas the electronic dipole $^4G_{5/2} \rightarrow {}^6H_{9/2}$ emission intensity is highly influenced by the local environment. The greater the intensity of the ED transition, the more asymmetric the nature of the local environment is.[69,70] The intensity ratio of $I(^4G_{5/2} \rightarrow {}^6H_{9/2})/I(^4G_{5/2} \rightarrow {}^6H_{5/2})$ could be employed as an indicator of the symmetry of the local environment of the Sm^{III} ion.[71] The intensity ratio is ca. 3.6, suggesting the low-symmetry coordination environments of Sm^{III} ions in **4**, which is in agreement with nonacoordinate severely distorted tricapped trigonal prism geometries of Sm^{III} ions. The excitation spectrum is dominated by the $^4G_{5/2} \rightarrow {}^6H_{9/2}$ transition, and the observable peaks can be attributed to the transitions from the $^6H_{5/2}$ ground state to $^6G_{9/2}$ (441 nm), $^6P_{5/2}$ (416 nm), $^4F_{7/2}$ (404 nm), $^4K_{11/2}$ (391 nm), $^6P_{7/2}$ (376 nm), and $^4L_{15/2}$ (363 nm) states (Figure 6b).[72] The decay profile of **4** taken by monitoring the $^4G_{5/2} \rightarrow {}^6H_{9/2}$ transition can be well-fitted by a double exponential function with lifetimes of τ_1 = 3.58 μs (12.35%) and τ_2 = 11.69 μs (87.65%), and the average lifetime of **4** is 10.68 μs (Figure 6c). The as-synthesized solid sample of **5** is measured under excitation at 395 nm, and its emission spectrum exhibits eight emission bands at 526, 534, 556, 579, 592, 615, 651, and 698 nm, which are severally assigned to the $^5D_1 \rightarrow {}^7F_0$, $^5D_1 \rightarrow {}^7F_1$, $^5D_1 \rightarrow {}^7F_2$, $^5D_0 \rightarrow {}^7F_0$, $^5D_0 \rightarrow {}^7F_1$, $^5D_0 \rightarrow {}^7F_2$, $^5D_0 \rightarrow {}^7F_3$, and $^5D_0 \rightarrow {}^7F_4$ transitions of the Eu^{3+} ions (Figure 6d). It is well-known that the $^5D_0 \rightarrow {}^7F_0$ transition is symmetry-forbidden emission in a field of symmetry, but the appearance of $^5D_0 \rightarrow {}^7F_0$ transition at 579 nm suggests that Eu^{3+} ions in **5** inhabit in a low symmetric ligand field, which is in good accordance with the heavily distorted tricapped triangular prism configurations. Generally speaking, the magnetic-dipolar $^5D_0 \rightarrow {}^7F_{1,3}$ transitions are independent of their local coordination environments, and the intensity of $^5D_0 \rightarrow {}^7F_1$ transition hardly changes with the ligand field strength exerted on the Eu^{3+} ion.[73,74] In contrast, the electro-dipolar $^5D_0 \rightarrow {}^7F_{0,2,4}$ transitions are rather hypersensitive to their local coordination environments, and the intensity of $^5D_0 \rightarrow {}^7F_2$ transition is extraordinarily dependent on the chemical bonds in the vicinity of the Eu^{3+} ion, whose intensity increases with the decrease of the site symmetry of the Eu^{3+} ion.[75] As a consequence, the intensity ratio of $^5D_0 \rightarrow {}^7F_2/{}^5D_0 \rightarrow {}^7F_1$ transitions is commonly utilized as a criterion to evaluate the coordination state and site symmetry of Eu^{3+} ions. In **5**, the intensity ratio is ca. 6.2, reflecting relatively low-symmetrical local environments of Eu^{3+} ions, coinciding well with the structural analysis. The excitation spectrum of **5** comprises four excitation bands, in which the intense band at 395 nm is attributed to the $^7F_0 \rightarrow {}^5L_6$ transition of the Eu^{3+} intra-$^4f_6$ ion, and three weak bands at 361, 380, and 415 nm are, respectively, assigned to $^7F_0 \rightarrow 5D_4$, $^7F_0 \rightarrow 5G_2$, and $^7F_0 \rightarrow {}^5D_3$ transitions (Figure 6e). The luminescent $^5D_0$ decay curve of **5** (Figure 6f) by monitoring at the strongest emission of the $^5D_0 \rightarrow {}^7F_2$ transition can be well-conformed to a double exponential function providing lifetimes of τ_1 = 116.54 μs (21.57%) and τ_2 = 264.81 μs (78.43%), indicating the existence of two distinct Eu^{3+} environments as is expected from the single-crystal structural determination. The average lifetime of **5** is calculated to be 232.83 μs. The intense and long-lived luminescence characteristics of the Eu^{III}-containing complexes allow for the applications in red-emitting glass materials. Upon photoexcitation at 367 nm, **7** emits green photoluminescence at room temperature and displays two evident emission bands at 488 and 543 nm as well as two weak emission bands at 582 and 618 nm, respectively. The three bands at 543, 582, and 618 nm are assigned to the $^5D_4 \rightarrow {}^7F_5$, $^5D_4 \rightarrow {}^7F_4$, and $^5D_4 \rightarrow {}^7F_3$ transitions of Tb^{3+} ions (Figure 6g).[76,77] To clarify the broad strong emission band at 485−493 nm in the emission spectrum of **7**, the PL emission behavior of **6** was investigated under the same condition as that of **7** (Figure S7a, Supporting Information), which does not display the luminescence emission in the visible range resulting from the stable half-filled f^7 electron configuration. An intense band around 475−485 nm is observed in the emission spectrum of **6**, which is induced by the $^3T_{1u} \rightarrow {}^1A_{1g}$ transition stemming from the O→W ligand-to-metal charge transfer (LMCT) of the $[B\text{-}\alpha\text{-}TeW_8O_{31}]^{10-}$ fragment. This observation indicates that the energy transfer from tungstotellurite polyoxoanion to Tb^{3+} ion probably may happen during the course of fluorescence emission process of **7**. Similar phenomenon have been already encountered.[78,79] The excitation spectrum of **7** obtained by monitoring the $^5D_4 \rightarrow {}^7F_5$ transition (543 nm) is dominated by the $^7F_5 \rightarrow {}^5D_2$ (367 nm) of the Tb^{III} intra-$^4f_8$ ions, whereas the other observable peaks are attributable to the transitions from the $^7F_6$ ground state to the excited states of $^5L_{10}$ at 352 nm, $^5G_6$ at 368 nm, and $^5D_3$ at 375 nm (Figure 6h).[77] In addition, the emission decay curve of **7** reveals a double exponential behavior, yielding the lifetime values of τ_1 = 1.00 μs (43.58%) and τ_2 = 8.60 μs (56.42%) (Figure 6i), and the average lifetime is calculated to be 5.29 μs. To further probe the contribution of $[B\text{-}\alpha\text{-}TeW_8O_{31}]^{10-}$ fragment in **7**, the lifetime decay curve of **6** was performed under similar conditions, which is also fitted by a double exponential function with τ_1 and τ_2 of 1.18 μs (45.91%) and τ_2 = 8.30 μs (54.09%) (Figure S7b, Supporting Information). The average lifetime of **6** is 5.03 μs, which is approximate to that of **7** (Figure S7c, Supporting Information). This result firmly proves that $[B\text{-}\alpha\text{-}TeW_8O_{31}]^{10-}$ segments make a nonignorable contribution to the PL behavior of **7** accompanying by the occurrence of the intramolecular energy transfer from O→W LMCT energy to Tb^{3+} centers during the emission procedure of **7**. In addition, the CIE chromaticity coordinates (x, y) determined on their corresponding PL spectra are found to be (0.528 02, 0.460 91) for **2**, (0.565 31, 0.426 81) for **4**, (0.656 62, 0.343 00) for **5**, and (0.271 66, 0.424 58) for **7**, respectively, which can be seen to be yellowish-red for **4**, red for **5**, and green for **7** (Figure S8, Supporting Information).

PL Properties of 4@CTAB Composites. To improve the PL emission properties of these crystalline materials, take **4** for example, we selected a cationic surfactant CTAB to cope with **4** to form **4@CTAB** composites and further explore the influences of the various mass ratio of CTAB/**4** on the PL

DOI: 10.1021/acs.inorgchem.7b00924
Inorg. Chem. 2017, 56, 7257−7269

emission properties of **4@CTAB** composites. CTAB usually functions, on the one hand, as the stabilizing agents allowing target materials chemical and mechanical inertness via capping the particle surfaces and preventing formed composites to agglomerate and, on the other hand, serves as regulating agents on the growth of composites for the well-defined morphology during the chemical syntheses.[80−85] Here, the SEM technique was employed to vividly describe the morphology of **4@CTAB** composites with the variable mass ratio of CTAB to **4** (Figure 7, Figure S9, Supporting Information). It is noticeable that the

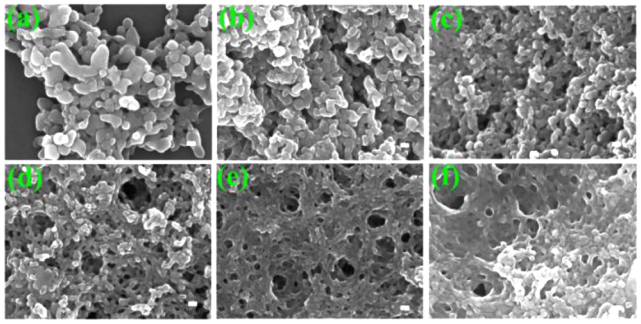

Figure 7. SEM images of **4@CTAB** composites with varying mass ratios of CTAB to **4** of 0.011/0.05 (a), 0.033/0.05 (b), 0.066/0.05 (c), 0.099/0.05 (d), 0.132/0.05 (e), and 0.165/0.05 (f) at a scale bar of 100 nm.

4@CTAB composite with the mass ratio of CTAB/**4** = 0.011/0.05 displays approximate peanutlike morphologies in the size of ca. 150 nm (Figure 7a). Improving the mass ratio of CTAB/**4** to 0.066/0.05, the **4@CTAB** composites become uniform with the smaller size of ∼100 nm (Figure 7b,c). However, upon continuously increasing the mass of CTAB, the morphologies of **4@CTAB** composites transform from the peanutlike shape to the honeycombed shape (Figure 7d−f). Thus, it can be found that the morphology of **4@CTAB** composites could be tuned neatly by the control of the CTAB/**4** ratio based on the experimental analyses. Besides, the fact that the polyoxoanionic skeleton of **4** remains unchanged in the formation of **4@CTAB** composites was also confirmed by the good agreements of the IR spectra of **4@CTAB** composites with the IR spectrum of **4** in the region of 1100−400 cm^{-1} (Figure S10, Supporting Information). For the pure CTAB, the absorption bands centered at 2850 and 2918 cm^{-1} are assigned to the C−H stretching vibrations, whereas the absorption bands appearing at 1431 and 1470 cm^{-1} are attributed to the C−H bending. Thus, the observed absorption peaks at 2854, 2922, and 1468 cm^{-1} suggest the presence of CTAB cations in the **4@CTAB** composites. Moreover, the minor shifts of corresponding peaks probably indicate the interactions of polyoxoanion **4** and CTAB.

The emission spectrum of **4** under the 404 nm excitation exhibits a series of characteristic bands of the Sm^{III} intra-$^4f_6$ transitions from $^4G_{5/2}$ to $^6H_{5/2}$ (561 nm), $^6H_{7/2}$ (596 nm), $^6H_{9/2}$ (644 nm), and $^6H_{11/2}$ (703 nm), respectively (Figure 8a). The emission spectra with different excitation wavelengths (EWs) of **4** were collected, and it can be clearly observed that the emission intensity is the strongest under the 404 nm excitation, which consolidates that the used EW is the most appropriate (Figure 8b). The introduction of the surfactant CTAB significantly will affect the morphology and the PL property of **4@CTAB** composites. To investigate the influence of the morphology of **4@CTAB** composites on the PL property, the solid-state PL properties of **4@CTAB** composites with various mass ratios of CTAB/**4** = 0/0.05, 0.011/0.05, 0.033/0.05, 0.066/0.05, 0.099/0.05, 0.132/0.05, and 0.165/0.05 were studied at ambient temperature. As illustrated in Figure 8c,d, the emission intensity increases gradually as the usage of CTAB increases (from 0/0.05 to 0.033/0.05), indicating that the small sizes of composites are beneficial to the luminescence enhancement. Furthermore, the strong interactions between CTAB and **4** can lead to the loss of coordination water molecules around Sm^{III} ions, and this relatively hydrophobic environment and the sensitization of CTAB toward the emission of Sm^{III} ions enhance the PL intensity.[86] Nevertheless, a further increase of the CTAB concentration (from 0.066/0.05 to 0.165/0.05) not only induces the visual change on their

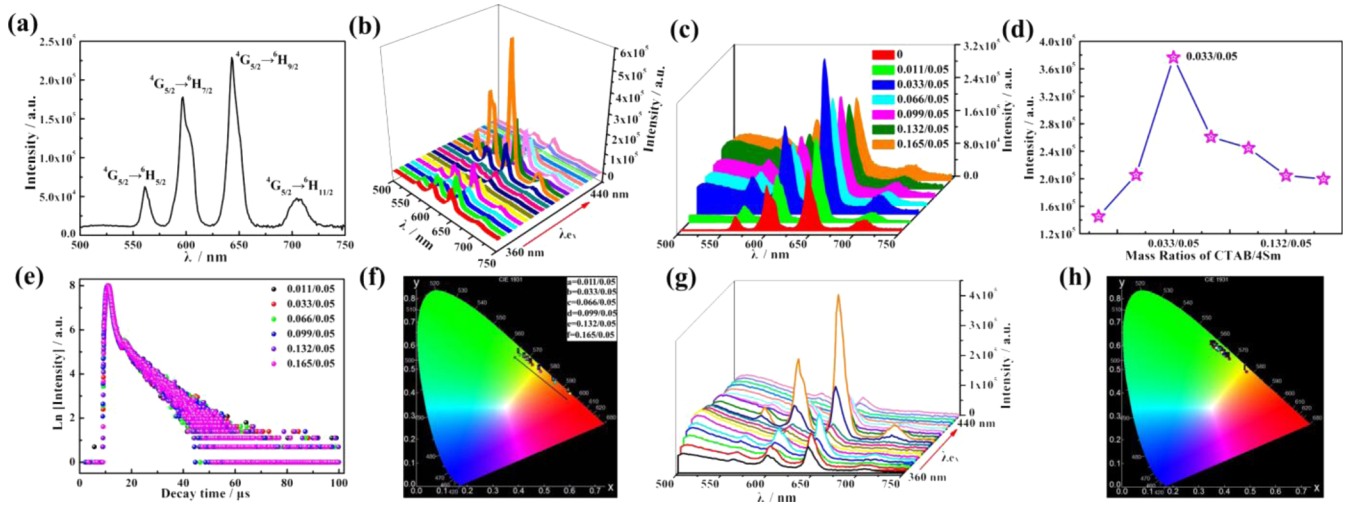

Figure 8. (a) The emission spectrum of **4** excited at 404 nm. (b) The emission spectra of **4** under various excitations from 360 to 440 nm with an interval of 4 nm. (c) The emission spectra of **4** and **4@CTAB** composites. (d) The variation of the PL emission intensity of the peak at 644 nm with the mass ratio of CTAB/**4**. (e) The decay curves of various **4@CTAB** composites obtained by monitoring the emission peak at 507 nm. (f) CIE chromaticity displaying the emission color change of various **4@CTAB** composites. (g, h) The emission spectra of **4@CTAB** composites with CTAB/**4** = 0.033/0.05 under various excitations from 360 to 440 nm with an interval of 4 nm and the corresponding CIE chromaticity.

DOI: 10.1021/acs.inorgchem.7b00924
Inorg. Chem. 2017, 56, 7257−7269

morphologies but also causes a sudden decline of the emission intensity (Figure 8c,d). This result may be related to the reason that a large amount of CTAB tightly wrapping the surface of **4** weakens the excitation intensity so as to impair the emission intensity of Sm^{III} ions. Noticeably, a new broad emission band of **4@CTAB** composites in the range of 500−550 nm immediately emerges as soon as CTAB was added into **4** (Figure S11, Supporting Information); moreover, the emission intensity of this band continuously ascends with the increasing concentration of CTAB. For the sake of verifying the origin of the new band, the PL behavior of CTAB was also studied under the same condition as **4@CTAB** composites (Figure S12, Supporting Information). It is apparent that the emission spectrum of CTAB displays an intense wide band at 510 nm, which may be induced by the intraligand charge-transfer (ILCT) process.[87,88] Therefore, the broad band located at 500−550 nm can be attributed to the ILCT of CTAB. The PL lifetime decay profiles of **4@CTAB** composites with varying mass ratios of CTAB/**4** by monitoring the strongest transition $^4G_{5/2}\rightarrow{}^6H_{9/2}$ were measured (Figure S13, Supporting Information), and all of them can be fitted to a second-order exponential function. The affording average lifetimes are summarized in Table S3 in the Supporting Information and illustrate a bit longer lifetimes of **4@CTAB** composites than **4**, which are probably attributed to the nanoscale effect of as-prepared materials,[89] different microenvironments causing the change of the site symmetry of the Sm^{III} ions, and the energy transfer from CTAB to the Sm^{III} centers. Moreover, the decay curve of pure CTAB also exhibits a second-order exponential function (Figure S14, Supporting Information), revealing the nonignorable contribution of CTAB in the emission process of **4@CTAB** composites, and this result can imply the occurrence of energy transfer from CTAB to the Sm^{III} centers. However, all the lifetimes of **4@CTAB** composites with the various mass ratios of CTAB/**4** are approximate, probably illuminating that the microenvironments of **4@CTAB** composite do not change much after the combination of CTAB with **4**. Additionally, the decay curves of the broad band around 507 nm of **4@CTAB** composites under the 404 nm excitation and the 507 nm emission conform to the second-order function with the average lifetimes of 5.48−5.89 μs (Figure 8e, Figure S15, Table S4, Supporting Information), which suggest that the lifetime contribution of CTAB in **4@CTAB** composites cannot be neglected. The corresponding CIE chromaticity coordinates of **4** and various **4@CTAB** composites are depicted in Figure 8f and Figure S16 in the Supporting Information. Obviously, the PL colors of **4@CTAB** composites can be tuned, which are exemplified by the emission colors changing from red, through yellow, to green by varying the mass ratio of CTAB/**4** from 0/0.05 to 0.264/0.05, associated with the CIE chromaticity coordinates from x = 0.605 32, y = 0.393 08, (red) to x = 0.410 38, y = 0.555 92 (green).

As shown in Figure 8c, the optimal mass ratio of CTAB/**4** = 0.033/0.05, in which the PL emission is the strongest, and this composite was selected for further investigation. Its emission spectra upon various EWs from 360 to 440 nm are demonstrated in Figure 3g, which indicate that the emission at 644 nm is maximum when the EW was 404 nm, in support with the above-mentioned examination of **4**. Upon increase in EW ranging from 360 to 404 nm, characteristic emission bands at 596 and 644 nm of Sm^{III} ions are obviously observed along with the intensity featuring a wavy change. Nonetheless, although the f−f transitions of Sm^{III} dominates the emission spectra collected at various EWs (360−416 nm), the emission intensity of the band around 507 nm always surpasses those of Sm^{III} ions, showing that ILCT emission is nonignorable. Noticeably, when EW is beyond 416 nm, the emission intensity derived from the Sm^{III} ions declines markedly, and characteristic peaks gradually vanish, whereas the peak intensity of CTAB is still enhanced, indicating that the ILCT emission predominates over the Sm^{III} emission. The CIE chromaticity diagram exhibits that the **4@CTAB** composite with CTAB/**4** = 0.033/0.05 mainly emits green emission with tiny disparity upon various EWs despite the yellowish emission is seen at the strongest EW of 404 nm (Figure 8h, Figure S17, Supporting Information). The TRES of **4** and **4@CTAB** composite with CTAB/**4** = 0.033/0.05) were measured in the spectral range of 500−750 nm with an interval of 2 nm under 404 nm excitation and sliced between 13 and 30 μs. Evidently, the TRES of **4** shows the typical peaks of Sm^{III} ions, and the emission intensity increases to the maximum at 16 μs and then presents an attenuated trend (Figure 9a). The emission spectral shape is

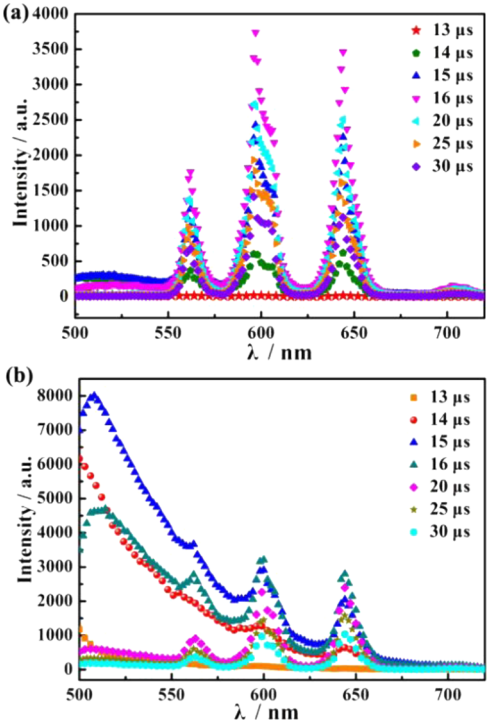

Figure 9. (a) The TRES of **4**. (b) The TRES of the **4@CTAB** composite with CTAB/**4** = 0.033/0.05.

not changeable, hinting that no obvious energy transfer phenomenon occurs in the emission process of **4**. Differently, a broad band derived from CTAB is observed in the TRES of the **4@CTAB** composite with CTAB/**4** = 0.033/0.05, and its intensity rapidly increases to the maximum at 15 μs and then drops; simultaneously, the intensity of the emission bands of Sm^{III} ions increases, revealing the occurrence of energy transfer from CTAB to Sm^{III} ions (Figure 9b), which further testifies that the substitution of coordination water molecules around Sm^{III} ions by CTAB surely occurs in the structure of the **4@CTAB** composite and that the sensitization of CTAB toward the emission of Sm^{III} ions enhances the PL intensity.

DOI: 10.1021/acs.inorgchem.7b00924
Inorg. Chem. 2017, 56, 7257−7269

4. CONCLUSION

In summary, a class of novel tellurotungstate-based organotin−RE heterometallic hybrids **1**−**7** with four organic ingredients were successfully prepared by the one-pot self-assembly reaction. Their polyoxoanionic skeletons consist of two symmetrical structural units $\{[Sn(CH_3)W_2O_4(IN)][(B\text{-}\alpha\text{-}TeW_8O_{31})RE(H_2O)\ (Ac)]_2\}^{10-}$ bridged by two acetate connectors. **1**−**7** not only represent the first inorganic−organic hybrid RE-substituted tellurotungstates involving three different organic ligands but also stand for the first inorganic−organic hybrid PBORHMs. The solid-state NIR PL properties of **2**, **3**, and **4** and visible PL properties of **2**, **4**, **5**, and **7** have been studied at room temperature. Furthermore, the morphologies of **4@CTAB** composites can be tuned by controlling the usage of CTAB. The PL properties of **4@CTAB** composites were intensively studied, which opens a new perspective for the design of POM-based optical nanomaterials. Future work will be extended to other PBORHMs functionalized by polycarboxylic ligands.

■ ASSOCIATED CONTENT

Supporting Information

The Supporting Information is available free of charge on the ACS Publications website at DOI: 10.1021/acs.inorgchem.7b00924.

BVS calculations of RE, Te, and W atoms; schematic synthetic procedure of **1**−**7**; related structural figures; PXRD patterns, UV spectra and TG curves of **1**−**7**; IR spectra of **1**−**7**, the free HIN ligand and K_2TeO_3; IR spectra and SEM images of **4@CTAB** composites; related luminescence spectra and luminescence decay curves; magnetic properties of **2**, **3**, and **4** (PDF)

Accession Codes

CCDC 1535527−1535533 contain the supplementary crystallographic data for this paper. These data can be obtained free of charge via www.ccdc.cam.ac.uk/data_request/cif, or by emailing data_request@ccdc.cam.ac.uk, or by contacting The Cambridge Crystallographic Data Centre, 12 Union Road, Cambridge CB2 1EZ, UK; fax: +44 1223 336033.

■ AUTHOR INFORMATION

Corresponding Authors

*E-mail: ljchen@henu.edu.cn. (L.-J. Chen)
*E-mail: zhaojunwei@henu.edu.cn. (J.-W. Zhao)
*E-mail: ygy@bit.edu.cn. (G.-Y. Yang)

ORCID

Jun-Wei Zhao: 0000-0002-7685-1309
Guo-Yu Yang: 0000-0002-0911-2805

Notes

The authors declare no competing financial interest.

■ ACKNOWLEDGMENTS

This work was supported by the National Natural Science Foundation of China (21671054, 21571048, 21301049, U1304208), the Innovation Scientists and Technicians Troop Construction Projects of Henan Province (174100510016), the Program for Science & Technology Innovation Talents in Universities of Henan Province (16HASTIT001), the Foundation of Education Department of Henan Province (16A150027), the Postdoctoral Foundation of Henan Province (20140025), the Foundation of State Key Laboratory of Structural Chemistry (20160016), the 2014 Special Foundation for Scientific Research Project of Henan Univ. (XXJC20140001), the 2012 Young Backbone Teachers Foundation from Henan Province (2012GGJS-027), and the Students Innovative Pilot Plan of Henan Univ. (16NA005).

■ REFERENCES

(1) Berzelius, J. Beitrag zur näheren Kenntniss des molybdäns. *Ann. Phys.* **1826**, *82*, 369−392.
(2) Kozhevnikov, I. V. Catalysis by heteropoly acids and multicomponent polyoxometalates in liquid-phase reactions. *Chem. Rev.* **1998**, *98*, 171−198.
(3) Hu, T.-P.; Zhao, Y.-Q.; Jagličić, Z.; Yu, K.; Wang, X.-P.; Sun, D. Four hybrid materials based on Preyssler P_5W_{30} polyoxometalate and first-row transition-metal complex. *Inorg. Chem.* **2015**, *54*, 7415−7423.
(4) Wang, S.-S.; Yang, G.-Y. Recent Advances in polyoxometalate-catalyzed reactions. *Chem. Rev.* **2015**, *115*, 4893−4962.
(5) Rhule, J. T.; Hill, C. L.; Judd, D. A.; et al. Polyoxometalates in medicine. *Chem. Rev.* **1998**, *98*, 327−358.
(6) Clemente-Juan, J. M.; Coronado, E.; Gaita-Ariño, A. Magnetic polyoxometalates: from molecular magnetism to molecular spintronics and quantum computing. *Chem. Soc. Rev.* **2012**, *41*, 7464−7478.
(7) Guo, L.-Y.; Zeng, S.-Y.; Jagličić, Z.; Hu, Q.-D.; Wang, S.-X.; Wang, Z.; Sun, D. A pyridazine-bridged sandwiched cluster incorporating planar hexanuclear cobalt ring and bivacant phosphotungstate. *Inorg. Chem.* **2016**, *55*, 9006−9011.
(8) Wang, Y. F.; Weinstock, I. A. Polyoxometalate-decorated nanoparticles. *Chem. Soc. Rev.* **2012**, *41*, 7479−7496.
(9) Song, Y.-F.; Tsunashima, R. Recent advances on polyoxometalate-based molecular and composite materials. *Chem. Soc. Rev.* **2012**, *41*, 7384−7402.
(10) Li, Y.-Wu.; Guo, L.-Y.; Su, H.-F.; Jagodič, M.; Luo, M.; Zhou, X.-Q.; Zeng, S.-Y.; Tung, C.-H.; Sun, Di.; Zheng, L.-S. Two unprecedented POM-based inorganic−organic hybrids with concomitant heteropolytungstate and molybdate. *Inorg. Chem.* **2017**, *56*, 2481−2489.
(11) Oms, O.; Dolbecq, A.; Mialane, P. Diversity in structures and properties of 3d-incorporating polyoxotungstates. *Chem. Soc. Rev.* **2012**, *41*, 7497−7536.
(12) Liang, M.-X.; Ruan, C.-Z.; Sun, D.; Kong, X.-J.; Ren, Y. P.; Long, L.-S.; Huang, R.-B.; Zheng, L.-S. Solvothermal synthesis of four polyoxometalate-based coordination polymers including diverse Ag(I)···π interactions. *Inorg. Chem.* **2014**, *53*, 897−902.
(13) Ma, X.; Li, H. L.; Chen, L. J.; Zhao, J. W. The main progress over the past decade and future outlook on high-nuclear transition-metal substituted polyoxotungstates: from synthetic strategies, structural features to functional properties. *Dalton Trans.* **2016**, *45*, 4935−4960.
(14) Zhao, Y.-Q.; Yu, K.; Wang, L.-W.; Wang, Y.; Wang, X.-P.; Sun, D. Anion-induced supramolecular isomerism in two Preyssler P_5W_{30} polyoxometalate-based hybrid materials. *Inorg. Chem.* **2014**, *53*, 11046−11050.
(15) Mialane, P.; Dolbecq, A.; Sécheresse, F. Functionalization of polyoxometalates by carboxylato and azido ligands: macromolecular complexes and extended compounds. *Chem. Commun.* **2006**, 3477−3485.
(16) Zhao, J.-W.; Li, Y.-Z.; Chen, L.-J.; Yang, G.-Y. Research progress on polyoxometalate-based transition-metal−rare-earth heterometallic derived materials: synthetic strategies, structural overview and functional applications. *Chem. Commun.* **2016**, *52*, 4418−4445.
(17) Dolbecq, A.; Dumas, E.; Mayer, C. R.; Mialane, P. Hybrid organic−inorganic polyoxometalate compounds: from structural diversity to applications. *Chem. Rev.* **2010**, *110*, 6009−6048.
(18) Proust, A.; Thouvenot, R.; Gouzerh, P. Functionalization of polyoxometalates: towards advanced applications in catalysis and materials science. *Chem. Commun.* **2008**, 1837−1852.
(19) Gong, P. J.; Li, Y. Y.; Zhai, C. P.; Luo, J.; Tian, X. M.; Chen, L. J.; Zhao, J. W. Syntheses, structural characterization and photophysical

DOI: 10.1021/acs.inorgchem.7b00924
Inorg. Chem. 2017, 56, 7257−7269

properties of two series of rare-earth-isonicotinic-acid containing Waugh-type manganomolybdates. *CrystEngComm* **2017**, *19*, 834−852.
(20) Coronado, E.; Yamashita, M. Molecular spintronics: the role of coordination chemistry. *Dalton Trans.* **2016**, *45*, 16553−16555.
(21) Gao, W. M.; Yu, T.; Wu, L. X.; Bi, L. H. Fabrication of white luminescence composite films containing Dy-polyoxometalate and the study of their luminescence switching behaviours. *Chem. Commun.* **2016**, *52*, 10403−10406.
(22) Li, H.-L.; Liu, Y.-J.; Liu, J.-L.; Chen, L.-J.; Zhao, J.-W.; Yang, G.-Y. Structural transformation from dimerization to tetramerization of serine-decorated rare-earth-incorporated arsenotungstates induced by the usage of rare-earth salts. *Chem. - Eur. J.* **2017**, *23*, 2673−2689.
(23) Sang, X. J.; Li, J. S.; Zhang, L. C.; Wang, Z. J.; Chen, W. L.; Zhu, Z. M.; Su, Z. M.; Wang, E. B. A novel carboxyethyltin functionalized sandwich-type germanotungstate: synthesis, crystal structure, photosensitivity, and application in dye-sensitized solar cells. *ACS Appl. Mater. Interfaces* **2014**, *6*, 7876−7884.
(24) Sang, X. J.; Li, J. S.; Zhang, L. C.; Zhu, Z. M.; Chen, W. L.; Li, Y. G.; Su, Z. M.; Wang, E. B. Two carboxyethyltin functionalized polyoxometalates for assembly on carbon nanotubes as efficient counter electrode materials in dye-sensitized solar cells. *Chem. Commun.* **2014**, *50*, 14678−14681.
(25) Zhang, B.; Zhang, L. C.; Zhang, Y. J.; Su, F.; You, W. S.; Zhu, Z. M. Two Keggin sandwich-type tungstophosphates modified by open-chain carboxyethyltin groups and transition metals. *RSC Adv.* **2015**, *5*, 47319−47325.
(26) Cao, R.; O'Halloran, K. P.; Hillesheim, D. A.; Lense, S.; Hardcastle, K. I.; Hill, C. L. Controlled synthesis of a functionalized polytungstate ligand and a $\{M_aM_bM_c(PW_9)_2\}$ sandwich complex. *CrystEngComm* **2011**, *13*, 738−740.
(27) Bai, J.-P.; Su, F.; Zhu, H.-T.; Sun, H.; Zhang, L.-C.; Liu, M.-Y.; You, W.-S.; Zhu, Z.-M. An open chain carboxyethyltin functionalized sandwich-type tungstophosphate based on a trivacant Dawson subunit: synthesis, characterization and properties. *Dalton Trans.* **2015**, *44*, 6423−6430.
(28) Bi, L.-H.; Hou, G.-F.; Li, B.; Wu, L.-X.; Kortz, U. Synthesis and crystal structure of pseudo-sandwich-type heteropolytungstates functionalized by organometallic ruthenium(II). *Dalton Trans.* **2009**, 6345−6353.
(29) Kortz, U.; Hussain, F.; Reicke, M. The ball-shaped heteropolytungstates $[\{Sn(CH_3)_2(H_2O)\}_{24}\{Sn(CH_3)_2\}_{12}(A\text{-}XW_9O_{34})_{12}]^{36-}$. *Angew. Chem., Int. Ed.* **2005**, *44*, 3773−3777.
(30) Hussain, F.; Kortz, U. Polyoxoanions functionalized by diorganotin groups: the tetrameric, chiral tungstoarsenate(III), $[\{Sn(CH_3)_2(H_2O)\}_2\{Sn(CH_3)_2\}As_3(\alpha\text{-}AsW_9O_{33})_4]^{21-}$. *Chem. Commun.* **2005**, 1191−1193.
(31) *SAINT V 6.01 (NT) Software for the CCD Detector System*; Bruker Analytical X-ray Systems: Madison, WI, 1999.
(32) Sheldrick, G. M. *SADABS: Program for Absorption Correction*; University of Göttingen: Göttingen, Germany, 1997.
(33) Sheldrick, G. M. *SHELXS 97, Program for Crystal Structure Solution*; University of Göttingen: Göttingen, Germany, 1997.
(34) Sheldrick, G. M. *SHELXL 97, Program for Crystal Structure Refinement*; University of Göttingen: Göttingen, Germany, 1997.
(35) Chen, W.-C.; Li, H.-L.; Wang, X.-L.; Shao, K.-Z.; Su, Z.-M.; Wang, E.-B. Assembly of cerium(III)-stabilized polyoxotungstate nanoclusters with SeO_3^{2-}/TeO_3^{2-} templates: from single polyoxoanions to inorganic hollow spheres in dilute solution. *Chem. - Eur. J.* **2013**, *19*, 11007−11015.
(36) Chen, W.-C.; Qin, C.; Wang, X.-L.; Li, Y.-G.; Zang, H.-Y.; Shao, K.-Z.; Su, Z.-M.; Wang, E.-B. Assembly of a large cerium(III)-containing tungstotellurites(IV) nanocluster: $[Ce_{10}Te_8W_{88}O_{298}(OH)_{12}(H_2O)_{40}]^{18-}$. *Dalton Trans.* **2015**, *44*, 11290−11293.
(37) Li, L.-L.; Han, H.-Y.; Wang, Y.-H.; Tan, H.-Q.; Zang, H.-Y.; Li, Y.-G. Construction of polyoxometalates from dynamic lacunary polyoxotungstate building blocks and lanthanide linkers. *Dalton Trans.* **2015**, *44*, 11429−11436.
(38) Ju, W.-W.; Zhang, H.-T.; Xu, X.; Zhang, Y.; Xu, Y. Enantiomerically pure lanthanide−organic polytungstates exhibiting two-photon absorption properties. *Inorg. Chem.* **2014**, *53*, 3269−3271.
(39) Vonci, M.; Akhlaghi Bagherjeri, F.; Hall, P. D.; Gable, R. W.; Zavras, A.; O'Hair, R. A. J.; Liu, Y. P.; Zhang, J.; Field, M. R.; Taylor, M. B.; Du Plessis, J.; Bryant, G.; Riley, M.; Sorace, L.; Aparicio, P. A.; López, X.; Poblet, J. M.; Ritchie, C.; Boskovic, C. Modular molecules: site-selective metal substitution, photoreduction, and chirality in polyoxometalate hybrids. *Chem. - Eur. J.* **2014**, *20*, 14102−14111.
(40) Chen, W. L.; Li, Y. G.; Wang, Y. H.; Wang, E. B.; Su, Z. M. Building block approach to nanostructures: step-by-step assembly of large lanthanide-containing polytungstoarsenate aggregates. *Dalton Trans.* **2007**, 4293−4301.
(41) Feng, X.-J.; Han, H.-Y.; Wang, Y.-H.; Li, L.-L.; Li, Y.-G.; Wang, E. B. Assembly of chainlike polyoxometalate-based lanthanide complexes in one-pot reaction system. *CrystEngComm* **2013**, *15*, 7267−7273.
(42) Ritchie, C.; Moore, E. G.; Speldrich, M.; Kögerler, P.; Boskovic, C. Terbium polyoxometalate organic complexes:correlation of structure with luminescence properties. *Angew. Chem., Int. Ed.* **2010**, *49*, 7702−7705.
(43) Hussain, F.; Gable, R. W.; Speldrich, M.; Kögerler, P.; Boskovic, C. Polyoxotungstate-encapsulated Gd_6 and Yb_{10} complexes. *Chem. Commun.* **2009**, 328−330.
(44) Ritchie, C.; Boskovic, C. Disassembly and reassembly of polyoxometalates: The formation of chains from an adaptable precursor. *Cryst. Growth Des.* **2010**, *10*, 488−491.
(45) Gaunt, A. J.; May, I.; Copping, R.; Bhatt, A. I.; Collison, D.; Fox, O. D.; Holman, K. T.; Pope, M. T. A new structural family of heteropolytungstate lacunary complexes with the uranyl, UO_2^{2+}, cation. *Dalton Trans.* **2003**, 3009−3014.
(46) Kalinina, I. V.; Izarova, N. V.; Kortz, U. Bis[tetraruthenium(IV)]- containing polyoxometalates: $[\{Ru^{IV}_4O_6(H_2O)_9\}_2Sb_2W_{20}O_{68}(OH)_2]^{4-}$ and $[\{Ru^{IV}_4O_6(H_2O)_9\}_2\{Fe(H_2O)_2\}_2\{\beta\text{-}TeW_9O_{33}\}_2H]^{-}$. *Inorg. Chem.* **2012**, *51*, 7442−7444.
(47) Ritchie, C.; Alley, K. G.; Boskovic, C. Lacunary tungstotellurates(IV): $[Te_2W_{17}O_{61}]^{12-}$, $[Te_2W_{16}O_{58}(OH)_2]^{14-}$ and $[Te_2W_{18}O_{62}(OH)_2]^{10-}$. *Dalton Trans.* **2010**, *39*, 8872−8874.
(48) Cameron, J. M.; Gao, J.; Long, D.-L.; Cronin, L. Self-assembly and structural transformations of high-nuclearity palladium-rich polyoxometalates. *Inorg. Chem. Front.* **2014**, *1*, 178−185.
(49) Ismail, A. H.; Nsouli, N. H.; Dickman, M. H.; Knez, J.; Kortz, U. The 20-Tungsto-4-tellurate(IV) $[H_2Te_4W_{20}O_{80}]^{22-}$ and the 15-tungstotellurate(IV) $[NaTeW_{15}O_{54}]^{13-}$. *J. Cluster Sci.* **2009**, *20*, 453−465.
(50) Gao, J.; Yan, J.; Beeg, S.; Long, D. L.; Cronin, L. Assembly of molecular "Layered" heteropolyoxometalate architectures. *Angew. Chem., Int. Ed.* **2012**, *51*, 3373−3376.
(51) Zheng, D.-M.; Wang, R.-Q.; Du, Y.; Hou, G.-F.; Wu, L.-X.; Bi, L.-H. A new organo-ruthenium substituted tungstotellurate: synthesis, structural characterization and catalytic properties. *New J. Chem.* **2016**, *40*, 8829−8836.
(52) Gao, J.; Yan, J.; Mitchell, S. G.; Miras, H. N.; Boulay, A. G.; Long, D.-L.; Cronin, L. Self-assembly of a family of macrocyclic polyoxotungstates with emergent material properties. *Chem. Sci.* **2011**, *2*, 1502−1508.
(53) Reinoso, S.; Bassil, B. S.; Barsukova, M.; Kortz, U. pH-Controlled assemblies of dimethyltin-functionalized 9-tungstophosphates with guanidinium as structure-directing cation. *Eur. J. Inorg. Chem.* **2010**, *2010*, 2537−2542.
(54) Reinoso, S.; Dickman, M. H.; Kortz, U. A novel hexatungstate fragment stabilized by dimethyltin groups: $[\{(CH_3)_2Sn\}_2(W_6O_{22})]^{4-}$. *Inorg. Chem.* **2006**, *45*, 10422−10424.
(55) Li, C. H.; Huang, K. L.; Chi, Y. N.; Liu, X.; Han, Z. G.; Shen, L.; Hu, C. W. Lanthanide−organic cation frameworks with zeolite gismondine topology and large cavities from intersected channels templated by polyoxometalate counterions. *Inorg. Chem.* **2009**, *48*, 2010−2017.

DOI: 10.1021/acs.inorgchem.7b00924
Inorg. Chem. 2017, 56, 7257−7269

(56) An, H.; Han, Z.; Xu, T. Three-dimensional architectures based on lanthanide-substituted double-Keggin-type polyoxometalates and lanthanide cations or lanthanide-organic complexes. *Inorg. Chem.* **2010**, *49*, 11403−11414.
(57) Den Auwer, C.; Charbonnel, M. C.; Drew, M. G. B.; Grigoriev, M.; Hudson, M. J.; Iveson, B. P.; Madic, C.; Nierlich, M.; Presson, M. T.; Revel, R.; Russell, M. L.; Thuery, P. Crystallographic, X-ray absorption, and IR studies of solid- and solution-state structures of tris(nitrato) N,N,N′,N′- tetraethylmalonamide complexes of lanthanides. comparison with the americium complex. *Inorg. Chem.* **2000**, *39*, 1487−1495.
(58) Niu, J. Y.; Wang, K. H.; Chen, H. N.; Zhao, J. W.; Ma, P. T.; Wang, J. Y.; Li, M. X.; Bai, Y.; Dang, D. B. Assembly chemistry between lanthanide cations and monovacant Keggin polyoxotungstates: two types of lanthanide substituted phosphotungstates $[\{(\alpha\text{-}PW_{11}O_{39}H)Ln(H_2O)_3\}_2]^{6-}$ and $[\{(\alpha\text{-}PW_{11}O_{39})Ln(H_2O)\ (\eta^2,\ \mu\text{-}1,1)\text{-}CH_3COO\}_2]^{10-}$. *Cryst. Growth Des.* **2009**, *9*, 4362−4372.
(59) Voloshin, A. I.; Shavaleev, N. M.; Kazakov, V. P. Luminescence of praseodymium (III) chelates from two excited states ($^3P_0$ and $^1D_2$) and its dependence on ligand triplet state energy. *J. Lumin.* **2001**, *93*, 199−204.
(60) Babai, A.; Mudring, A. V. Anhydrous praseodymium salts in the ionic liquid [bmpyr][Tf_2N]: structural and optical properties of [bmpyr]$_4$[PrI_6][Tf_2N] and [bmyr]$_2$[$Pr(Tf_2N)_5$]. *Chem. Mater.* **2005**, *17*, 6230−6238.
(61) Dang, S.; Yu, J. B.; Wang, X. F.; Sun, L. N.; Deng, R. P.; Feng, J.; Fan, W. Q.; Zhang, H. J. NIR-luminescence from ternary lanthanide [Ho^{III}, Pr^{III} and Tm^{III}] complexes with 1-(2-naphthyl)-4,4,4-trifluoro-1,3-butanedionate. *J. Lumin.* **2011**, *131*, 1857−1863.
(62) Fujii, T.; Kodaira, K.; Kawauchi, O.; Tanaka, N.; Yamashita, H.; Anpo, M. Photochromic behavior in the fluorescence spectra of 9-anthrol encapsulated in Si−Al glasses prepared by the sol−gel method. *J. Phys. Chem. B* **1997**, *101*, 10631−10637.
(63) Veith, M.; Belot, C.; Huch, V.; Cui, H. L.; Guyard, L.; Knorr, M.; Wickleder, C. Synthesis, crystal structure and physico-chemical studies of neodymium and erbium methoxides containing thienyl substituents. *Eur. J. Inorg. Chem.* **2010**, *2010*, 879−889.
(64) Abdelhameed, R. M.; Carlos, L. D.; Silva, A. M. S.; Rocha, J. Near-infrared emitters based on post-synthetic modified Ln^{3+}-IRMOF-3. *Chem. Commun.* **2013**, *49*, 5019−5021.
(65) Klink, S. I.; Alink, P. O.; Grave, L.; Peters, F. G. A.; Hofstraat, J. W.; Geurts, F.; van Veggel, F. C. J. M. Fluorescent dyes as efficient photosensitizers for near-infrared Nd^{3+} emission. *J. Chem. Soc., Perkin Trans.* **2001**, *2*, 363−372.
(66) Sun, L. N.; Qiu, Y. N.; Liu, T.; Zhang, J. Z.; Dang, S.; Feng, J.; Wang, Z. J.; Zhang, H. J.; Shi, L. Y. Near infrared and visible luminescence from xerogels covalently grafted with lanthanide [Sm^{3+}, Yb^{3+}, Nd^{3+}, Er^{3+}, Pr^{3+}, Ho^{3+}] β- diketonate derivatives using visible light excitation. *ACS Appl. Mater. Interfaces* **2013**, *5*, 9585−9593.
(67) Sun, L.-N.; Zhang, Y.; Yu, J.-B.; Peng, C.-Y.; Zhang, H.-J. Ternary lanthanide (Er^{3+}, Nd^{3+}, Yb^{3+}, Sm^{3+}, Pr^{3+}) complex-functionalized mesoporous SBA-15 materials that emit in the near-infrared range. *J. Photochem. Photobiol., A* **2008**, *199*, 57−63.
(68) Lenaerts, P.; Driesen, K.; Van Deun, R.; Binnemans, K. Covalent coupling of luminescent tris(2-thenoyltrifluoroacetonato)-lanthanide(III) complexes on a merrifield resin. *Chem. Mater.* **2005**, *17*, 2148−2154.
(69) Jamalaiah, B. C.; Suresh Kumar, J.; Mohan Babu, A.; Suhasini, T.; Rama Moorthy, L. Photoluminescence properties of Sm^{3+} in LBTAF glasses. *J. Lumin.* **2009**, *129*, 363−369.
(70) Xia, X.-L.; Ouyang, J.-H.; Liu, Z.-G. Electrical properties of gadolinium−europium zirconate ceramics. *J. Am. Ceram. Soc.* **2010**, *93*, 1074−1080.
(71) Brito, H. F.; Malta, O. L.; Felinto, M. C. F. C.; Teotonio, E. E. S.; Menezes, J. F. S.; Silva, C. F. B.; Tomiyama, C. S.; Carvalho, C. A. A. Luminescence investigation of the Sm(III)-β-diketonates with sulfoxides, phosphine oxides and amides ligands. *J. Alloys Compd.* **2002**, *344*, 293−297.
(72) Meza-Rocha, A. N.; Speghini, A.; Bettinelli, M.; Caldiño, U. Orange and reddish-orange light emitting phosphors: Sm^{3+} and Sm^{3+}/Eu^{3+} doped zinc phosphate glasses. *J. Lumin.* **2015**, *167*, 305−309.
(73) Li, C. C.; Liu, S. X.; Li, S. J.; Yang, Y.; Jin, H. Y.; Ma, F. J. Assembly of saturated Nb/W mixed-addendum polyoxometalate $[P_2W_{15}Nb_3O_{62}]^{9-}$ and lanthanide ions (Ln = Eu, Ce). *Eur. J. Inorg. Chem.* **2012**, *2012*, 3229−3234.
(74) Xu, Q. H.; Li, L. S.; Liu, X. S.; Xu, R. R. Incorporation of rare-earth complex $Eu(TTA)_4C_5H_5NC_{16}H_{33}$ into surface-modified Si−MCM-41 and its photophysical properties. *Chem. Mater.* **2002**, *14*, 549−555.
(75) Choppin, G. R.; Peterman, D. R. Applications of lanthanide luminescence spectroscopy to solution studies of coordination chemistry. *Coord. Chem. Rev.* **1998**, *174*, 283−299.
(76) Xia, J.; Zhao, B.; Wang, H.-S.; Shi, W.; Ma, Y.; Song, H. B.; Cheng, P.; Liao, D. Z.; Yan, S. P. Two- and three-dimensional lanthanide complexes: synthesis, crystal structures, and properties. *Inorg. Chem.* **2007**, *46*, 3450−3458.
(77) Choi, Y. I.; Yoon, Y.; Kang, J.-G.; Sohn, Y. Photoluminescence imaging of Eu(III) and Tb(III)-embedded SiO_2 nanostructures. *J. Lumin.* **2015**, *158*, 27−31.
(78) Ito, T.; Yashiro, H.; Yamase, T. Regular Two-dimensional molecular array of photoluminescent Anderson-type polyoxometalate constructed by Langmuir−Blodgett technique. *Langmuir* **2006**, *22*, 2806−2810.
(79) Chen, L. J.; Zhang, F.; Ma, X.; Luo, J.; Zhao, J. W. Two types of novel tetra-iron substituted sandwich-type arsenotungastates with supporting lanthanide pendants. *Dalton Trans.* **2015**, *44*, 12598−12612.
(80) Liu, M. Z.; Guyot-Sionnest, P. Mechanism of silver(I)-assisted growth of gold nanorods and bipyramids. *J. Phys. Chem. B* **2005**, *109*, 22192−22200.
(81) Liu, X. H.; Luo, X. H.; Lu, S. X.; Zhang, J. C.; Cao, W. L. A novel cetyltrimethyl ammonium silver bromide complex and silver bromide nanoparticles obtained by the surfactant counterion. *J. Colloid Interface Sci.* **2007**, *307*, 94−100.
(82) Zhao, Y. Y.; Fan, H. M.; Li, W.; Bi, L. H.; Wang, D. J.; Wu, L. X. Incorporation of polyoxotungstate complexes in silica spheres and in situ formation of tungsten trioxide nanoparticles. *Langmuir* **2010**, *26*, 14894−14900.
(83) Fu, Q.; Ran, G. J.; Xu, W. L. Direct self-assembly of CTAB-capped Au nanotriangles. *Nano Res.* **2016**, *9*, 3247−3256.
(84) Jiang, Y. Q.; Zhao, Y.; Xu, X. Z.; Lin, K. F.; Wang, D. Mesoporous titanosilicate nanoparticles: facile preparation and application in heterogeneous epoxidation of cyclohexene. *RSC Adv.* **2016**, *6*, 77481−71488.
(85) Zhao, J. W.; Xu, P. Y.; Li, Y.; Wu, J.; Xue, J. F.; Zhu, Q. N.; Lu, X. X.; Ni, W. H. Direct coating of mesoporous titania on CTAB-capped gold nanorods. *Nanoscale* **2016**, *8*, 5417−5421.
(86) Zhang, T.; Li, H.-W.; Wu, Y. Q.; Wang, Y. Z.; Wu, L. X. Self-assembly of an europium-containing polyoxometalate and the arginine/lysine-rich peptides from human papillomavirus capsid protein L1 in forming luminescence-enhanced hybrid nanoparticles. *J. Phys. Chem. C* **2015**, *119*, 8321−8328.
(87) Yang, Q.-Y.; Pan, M.; Wei, S.-C.; Li, K.; Du, B.-B.; Su, C.-Y. Linear dependence of photoluminescence in mixed Ln-MOFs for color tunability and barcode application. *Inorg. Chem.* **2015**, *54*, 5707−5716.
(88) Yang, Q.-Y.; Wu, K.; Jiang, J.-J.; Hsu, C.-W.; Pan, M.; Lehn, J.-M.; Su, C.-Y. Pure white-light and yellow-to-blue emission tuning in single crystals of Dy(III) metal−organic frameworks. *Chem. Commun.* **2014**, *50*, 7702−7704.
(89) Zhao, Y. L.; Zhou, D. J.; Yao, G. Q.; Huang, C. H. Strong luminescent Terbium(III)−pyrazolone complexes and their langmuir−blodgett films. *Langmuir* **1997**, *13*, 4060−4065.

DOI: 10.1021/acs.inorgchem.7b00924
Inorg. Chem. 2017, 56, 7257−7269